



Fast Reference-free Crack Measurement (RACM) System in Transportation Infrastructures using Non-Contact Ultrasound

Suyun Ham



FINAL REPORT

FAST REFERENCE-FREE CRACK MEASUREMENT (RACM) SYSTEM IN TRANSPORTATION INFRASTRUCTURES USING NONCONTACT ULTRASOUND

FINAL PROJECT REPORT

by

Suyun Ham
The University of Texas at Arlington

Sponsorship

(List CTEDD and matching external sponsors, e.g. WSDOT)

for

Center for Transportation, Equity, Decisions and Dollars (**CTEDD**)
USDOT University Transportation Center
The University of Texas at Arlington
601 W.Nedderman Dr. Suite 103
Arlington TX 76019-0108 United States
Phone: 817-272-5138 | Email: C-Tedd@uta.edu

In cooperation with US Department of Transportation-Research and

Acknowledgment

This work was supported by a grant from the Center for Transportation Equity, Decisions and Dollars (CTEDD) funded by U.S. Department of Transportation Research and Innovative Technology Administration (OST-R) and housed at The University of Texas at Arlington.

Disclaimer

The contents of this report reflect the views of the authors, who are responsible for the facts and the accuracy of the information presented herein. This document is disseminated under the sponsorship of the U.S. Department of Transportation's University Transportation Centers Program, in the interest of information exchange. The Center for Transportation, Equity, Decisions and Dollars (CTEDD), the U.S. Government and matching sponsor assume no liability for the contents or use thereof

Technical Report Documentation Page

1. Report No.	2. Government Accession No.	3. Recipient's Catalog No.	
4. Title and Subtitle Fast Reference-free Crack Measurement (RACM) System in Transportation Infrastructures using Non-contact Ultrasound		5. Report Date	
		6. Performing Organization Code	
7. Author(s) Suyun Ham		8. Performing Organization Report No.	
9. Performing Organization Name and Address Center for Transportation, Equity, Decisions, and Dollars (CTEDD) USDOT University Transportation Center The University of Texas at Arlington 601 W.Nedderman Dr. Suite 103 Arlington TX 76019-0108 United States		10. Work Unit No. (TRAIS)	
		11. Contract or Grant No.	
12. Sponsoring Organization Name and Address United States of America Department of Transportation Research and Innovative Technology Administration		13. Type of Report and Period Covered	
		14. Sponsoring Agency Code	
15. Supplementary Notes Report uploaded at www.ctedd.uta.edu			
16. Abstract <p>According to a 2017 report by the American Society of Civil Engineers, the infrastructure of the United States requires a \$2.0 trillion investment to return it to good condition by 2025. Distributed microcracks and delaminated damages in our transportation system's concrete infrastructure have caused more deterioration by cracks and more delamination by corrosion, adversely affecting the system components' mechanical strength, stiffness, and permeability. Freeze and Thaw (F&T) and Alkalis Silica Reaction (ASR) are the most common cause of the microcrack formation in the concrete infrastructures. The early detection of these propagating damages through a pragmatic non-destructive testing technique can lead to a better decision making which prevent further degradation and saves money, time, and lives.</p> <p>As of today, there is no NDT method that have proven to be sensitive on the early stage damages such as F&T in an inhomogeneous infrastructure. The methods are either insensitive to early stages (low crack volumes) of damage, not repeatable, or inconsistent. Prior methods have had an inadequate contact system that cannot measure the damage quickly enough as they require a contact to the surface, and a more sophisticated reference data system that can more readily respond to the nature of the heterogeneous aspects of the problem sites.</p> <p>This research presents the solution in the form of a reference-free acoustic crack measurement (RACM) system. The developed RACM system provides absolute damage index values. The RACM utilizes non-contact ultrasonic system to implement backscattering waves to characterize the damage level. Three F&T damaged specimens were prepared and tested with the RACM and other techniques such as resonant frequency tests and expansion tests in a laboratory. The research presents the results of the field tests using the ultrasonic sensor array device (MIRA) and RACM system. In addition, website-based and App-based monitoring platforms are developed to allow fast access to the test results using map-based location displayer.</p>			
17. Key Words Noncontact Ultrasound, Crack measurement, Backscattering waves		18. Distribution Statement No restrictions.	
19. Security Classification (of this report) Unclassified.	20. Security Classification (of this page) Unclassified.	21. No. of Pages 79	22. Price NA

Table of Contents

Table of Contents	6
List of Figures	8
List of Tables.....	11
Exclusive summary	12
1. Introduction	13
1.1. Background & Theory	14
1.2. Instrumentations.....	17
1.2.1. Mechanical strain gauge	17
1.2.2. Data Acquisition (DAQ) system.....	17
1.2.3. Sensors.....	18
1.2.4. Pre-Amplifier.....	19
1.2.5. Transmitter.....	20
1.2.6. Contact 3D tomographic ultrasound (MIRA).....	20
1.3. Device Developments	21
1.3.1. RACM handheld device development.....	21
1.3.2. Freeze and Thaw Machine.....	22
2. Numerical Analyses	24
2.1. Finite element resonant frequency analysis:.....	24
2.2. Finite element 2D random shape of aggregate model using image processing and convex combination theory.....	25
2.2.1. Methodology.....	25
2.2.2. Procedure of random aggregate generation.....	27
2.2.3. Results and discussions	32
3. Specimen Preparation and Parametric study.....	35
3.1. Specimens	35
3.2. Concrete Designs	36
3.3. Freeze and thaw test:.....	38
3.4. RACM sensor’s sensitivity measurement.....	39
4. Test Procedures	41
4.1. Test Procedure’s Overview.....	41
4.2. Expansion Measurement.....	41
4.3. Resonant frequency test	43

4.4.	RACM Measurement	44
4.5.	MIRA Test	45
5.	System Analysis Software Development	47
5.1.	Methodology: Mobile Android APP.....	47
5.2.	Methodology: web-based platform.....	48
5.3.	Design and process	49
6.	Results and Discussion.....	57
6.1.	Laboratory Tests	57
6.1.1.	Expansion test:.....	57
6.1.2.	Resonant frequency test:.....	58
6.1.3.	RACM (IBS) test:.....	59
6.2.	Field Tests.....	61
6.2.1.	Parking lots	64
6.2.2.	Bridge road:	66
6.2.3.	Pedestrian:	62
7.	Conclusions and Recommendations.....	72
8.	References	73
	<i>Appendix A – Fitted Curve Coefficients</i>	<i>75</i>
	<i>Appendix B – Procedures for Android App.....</i>	<i>78</i>

List of Figures

Figure 1. Scanning of Electron Microscopy (SEM) image of concrete specimen subjected to frost condition [3].....	13
Figure 2. Mechanical waves particle motions.....	15
Figure 3. The reflection of ultrasonic energy away from the original direction of propagation, caused by reflection, refraction, and mode conversion from internal inclusions. Causes of signal loss include signal dispersion and scattering “noise”.	16
Figure 4. The Demountable Mechanical Strain Gauge (DEMEC): 300 mm DEMEC (left), 1mm drilled stainless steel disks and bolt (right).....	17
Figure 5. DAQ system: PicoScope TC-08 USB for acquisition of the thermocouples signals (left), PicoScope 4842 for acquisition of the accelerometers and the MEMS sensor’s signals (right)	18
Figure 6. Piezoelectric sensor for vibration measurement.....	18
Figure 7. MEMS sensor: schematic and design layout of the MEMS sensor (left), the produced MEMS sensor using SPM0404UD5 microphones (right)	19
Figure 8. The thermocouple sensors: thermocouple wires (left), thermocouple connectors (right)	19
Figure 9. Kistler 5134B signal conditioner.....	20
Figure 10. 50 kHz ultrasonic transmitter	20
Figure 11. Contact tomography system (MIRA): (left) linear arrayed sensor in MIRA on concrete sample, and (right) 3-D representation of internal defects by MIRA system.....	21
Figure 12. RACM handheld device: the RACM handheld device configuration (top), the schematic of the sensors’ configuration in the RACM handheld device (bottom left), the developed PCB for backward MEMS sensors with BNC cable output (bottom right).....	22
Figure 13. Freeze and thaw machine: the schematic of the F&T machine (left), and the freezer, heating elements and the tray (right).	23
Figure 14. Resonant frequency result of prism specimen: the resonant frequency test (left), and the FEM simulation for Eigen-value analysis (right).	24
Figure 15. Resonant frequency result of slab specimen: the resonant frequency test (left), and the FEM simulation for Eigen-value analysis (right).	24
Figure 16. Procedure of the aggregate similarity check using cross-correlation and Hausdorff distance method by detecting the the best rotation angle: (a) Cross correlation method and (b) Hausdorff distance method.....	26
Figure 17. Digital image processing procedure: (a) Sample preparation, (b) image digitalization, (c) image registration, (d) edge detection using Sobel approximation and centroid determination for the rotation procedure, and (e) coordinate conversion from polar to Cartesian.	28
Figure 18. Presentation of the generated aggregate in a polar curve (a) and its signature curve (b).	29
Figure 19. Statistical studies on the aggregates: to determine type based on the aspect ratio (left) and distribution of the thresholds from 10 sets (right).....	30
Figure 20. Aggregate analysis of distribution of the aggregates in the groups (left) and curve fitting for the aggregate signature curve (right).....	32

Figure 21. Normalized randomly generated aggregates for the round (left column), crushed (middle column), and needle shape (right column), where the largest diameter of aggregates is limited to 1.	33
Figure 22. The selection of an arbitrary aggregate as a reference from other studies (31) and conveying the aggregate into a FE analysis model to compare with the three main aggregate models: Circle, hexagonal, and the proposed random shape aggregate.....	34
Figure 23. Time domain signal (a) Ultrasonic wave propagation signal from the FE analysis for no aggregate, reference, CCT-RSAM, circle, and hexagonal aggregates and (b) zoomed in the plot in the circle from FIGURE (a).....	34
Figure 24. The backscattering energy of the reference, CCT-RSAM, circle, and hexagonal aggregates	35
Figure 25. Sample preparation: the mold preparation (top), specimens actual size (bottom left), and the thermocouple location for slabs, FT1, FT2, FT3, and control (bottom right)...	37
Figure 26. Thermocouple’s positions for the TC Control specimen: the 3D view of the location of thermocouples at 1, 7, and 14 cm deep inside the specimen (left), and top view of the thermocouple’s positions (right).	38
Figure 27. Freeze and thaw cycle with procedure B during the three days.	39
Figure 28. The advantage of using baffles to delay the sound wave arrival.....	40
Figure 29. Resonant frequency test schematic.....	44
Figure 30. The RACM testing layout on the slab specimens	45
Figure 31. MIRA testing direction (left) and field test picture.....	46
Figure 32 Case diagram for the main screen	49
Figure 33 Case diagram for the menu screen	50
Figure 34. screen shot of the XML code : Relative layout for Android Google maps.....	50
Figure 35. API key.....	51
Figure 36. Back-end Java code	52
Figure 37. Google map with the marked five different locations.....	52
Figure 38. Calendar window: code using ‘setOnMarkerClickListener’ (left) and screen shot of date selection window (right)	52
Figure 39. Specimen selection window	53
Figure 40. Example of test result code (top) and IBS (RACM) test result window (bottom)	54
Figure 41. Linear layout function	55
Figure 42. Plotting graph Java code.....	55
Figure 43. While loop (left) and declaration (right) of Java script to create arrays.....	56
Figure 44. Example of expansion test result.....	56
Figure 45. Expansion test result of the control slab specimen.....	57
Figure 46. Expansion test result of the control specimen: FT1 (top), FT2 (middle), and FT3 (bottom).....	57
Figure 47. Surface of cycled prism concrete specimen, PT1.....	58
Figure 48. Resonant frequency test result of prism specimen	58
Figure 49. Resonant frequency test result of concrete specimens	59
Figure 50. Waveforms of mechanical waves of PMMA, FT3, and control specimen	Error!
	Bookmark not defined.
Figure 51. Energy boxplot of specimens	Error! Bookmark not defined.
Figure 52. Backscattered of CTS, FT2, FT3, and PMMA specimen.....	60
Figure 53. Energy boxplot of specimens	60

Figure 54. Backscattered energy and resonant frequency tendency of laboratory test specimens 61

Figure 55. Site of parking lots: satellite map (left) and site photo (right) 65

Figure 56. RACM (left) and MIRA (right) test on the parking lot site 65

Figure 57. MIRA result image on the parking lot site 65

Figure 58. Backscattered waves and energy boxplot of parking lot site 66

Figure 59. Site of bridge road: satellite map (left) and site photo (right) 67

Figure 60. RACM (left) and MIRA (right) test on the bridge deck..... 67

Figure 61. MIRA result image on the parking lot site of bridge site 67

Figure 62. Backscattered waves and energy boxplot of bridge site..... 68

Figure 63. Site of pedestrian: satellite map (left) and site photo (right) 62

Figure 64. Pedestrian condition: old pedestrian (left) and recently constructed pedestrian (right) 62

Figure 65. RACM (left) and MIRA (right) test on the pedestrian concrete pavement 63

Figure 66. MIRA result image on the pedestrian: existing pedestrian (left) and recently constructed pedestrian (right)..... 63

Figure 67. Backscattered waves of pedestrian sites: existing pedestrian (left) and recently constructed pedestrian (right) 64

List of Tables

Table 1. The mechanical wave's properties [8]	15
Table 2. Specimens' size	36
Table 3. Concrete mix design.....	36
Table 4. Specimens' physical properties after casting.....	37
Table 5 Temperature changes of two cycles for one week	38
Table 6. Test procedure	41
Table 7. Resonant frequency test parameters	43
Table 8. RACM test parameters	45
Table 9. The steps to acquire the Android Google maps key.....	50

Exclusive summary

According to a 2017 report by the American Society of Civil Engineers, the infrastructure of the United States requires a \$2.0 trillion investment to return it to good condition by 2025. Distributed microcracks and delaminated damages in our transportation system's concrete infrastructure have caused more deterioration by cracks and more delamination by corrosion, adversely affecting the system components' mechanical strength, stiffness, and permeability. Freeze and thaw (F&T) and Alkaline Silica Reaction (ASR) are the most common cause of the microcrack formation in the concrete infrastructures. The early detection of these propagating damages through a pragmatic non-destructive testing technique can lead to a better decision making which prevent further degradation and saves money, time, and lives.

In existence of water in the porous media, e.g. concrete, the jeopardy of microcrack formation is always an issue with the temperature variation, e.g. F&T. The freezing temperature causes ice crystallization in the pores. The produced ice crystals, in existence of the super-cooled water increase the pressure on the pore's walls and leads to crack formation. In regards repetition of these procedures can significantly damage the concrete over them.

As of today, there is no NDT method that have proven to be sensitive on the early stage damages such as F&T in an inhomogeneous infrastructure. The methods are either insensitive to early stages (low crack volumes) of damage, not repeatable, or inconsistent. Prior methods have had an inadequate contact system that cannot measure the damage quickly enough as they require a contact to the surface, and a more sophisticated reference data system that can more readily respond to the nature of the heterogeneous aspects of the problem sites.

This research presents the solution in the form of a reference-free acoustic crack measurement (RACM) system. The developed RACM system provides absolute damage index values. The RACM utilizes non-contact ultrasonic system to implement backscattering waves to characterize the damage level. Three F&T damaged specimens were prepared and tested with the RACM and other techniques such as resonant frequency tests and expansion tests in a laboratory. The research presents the results of the field tests using the ultrasonic sensor array device (MIRA) and RACM system. In addition, website-based and App-based monitoring platforms are developed to allow fast access to the test results using map-based location displayer.

1. Introduction

The infrastructure growth in the United States has come at the expense of long-term durability for the concrete structures. Unrestraint implementation of general-purpose concrete mix has significantly increased the pace of concrete infrastructure constructions; however, it made the concrete structures vulnerable to the environmental degradations such as freeze and thaw (F&T). According to the Federal Highway Administration (FHWA), the life cycle of the pavements subjected to freezing condition is significantly lower than the pavements with no exposure to the frost condition which costs millions of dollars for the U.S. Department of Transportations (DOTs) every year [1]. For instance, in 2018 the estimated value of the affected transportation structure in the Houston District of the Texas DOT was about 1 billion dollar [2]. The frost condition, i.e. F&T, of the environment causes the formation of the networks of microcrack in the concrete structures. Figure 1 shows the Scanning Electron Microscopy (SEM) image of a concrete specimen subjected to the frost condition which shows the crack propagation in the concrete [3]. These microcracks under the continues frost condition will further turn into a major crack, Moreover, these network microcracks adversely affect the concrete material mechanical strength, strength, and permeability. In addition, these cracks make the concrete more vulnerable to the ingress of aggressive substances. Early stage detection of these microcracks is the main concern of the USDOTs, where with an implementation of a proper non-destructive technique the vulnerable infrastructures can be detected prior to the occurrence of the major damages.

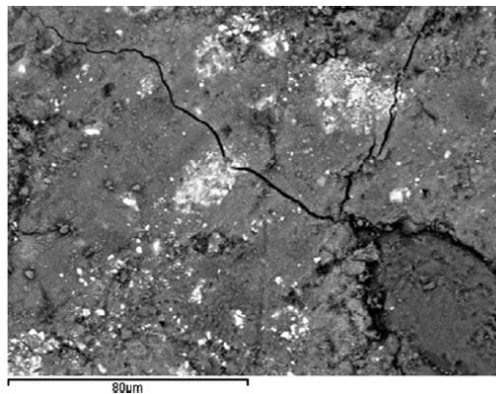


Figure 1. Scanning of Electron Microscopy (SEM) image of concrete specimen subjected to frost condition [3]

Damage type detection is crucially important for preventive maintenance, and correct decision making for proper repair of the damaged reinforced concrete and other transportation infrastructures. As of today, there is no non-destructive testing (NDT) method to be able to detect and differentiate the different types of concrete degradation. Giannini *et.al.* in 2012 conducted research with collaboration of The University of Texas at Austin, Texas A&M University, and the Texas Department of Transportation (TxDOT) to investigate the effectiveness of the conventional NDT techniques and devices such as Ultrasonic Pulse Velocity (UPV), Impact-Echo, Spectral Analysis of Surface Waves (SASW), resonant frequency test, and nonlinear acoustics [4]. The results showed that none of the methods are efficiently able to detect microcracks damage.

Clyton *et.al.* reported to the Oak Ridge National Laboratory in 2016, the efficiency of a ultrasonic sensor array device, called MIRA, and the implementation of Hilbert Transform Indicator (HTI) for quantification of F&T in concrete structures. Although their results are promising to some extent but due to the nature of their contact system, the scanning procedure is noticeably slow, which unable their technique to be practical for vast field Application.

In this research the sensitivity of a reference-free acoustic crack measurement (RACM) technique is investigated and compared with the two most sensitive NDT methods to the early stage cracks, i.e., resonant frequency test and MIRA. The number of four concrete slabs were prepared and subjected to F&T cycles through a developed F&T machine. The expansion measurement test was carried out to monitor the expansion of the specimen at different cycles.

The era of mobile technology opens the windows to the Android App. Websites are vanishing, and the mobile phones are emerging. It's the time to change from conventional websites to Apps, which has become the part of our daily routine. "SMTL.apk" Android Application software is introduced. The main aim of the mobile App is to allow fast access of our hardware remotely and to provide a user-friendly environment to access, monitor, and control operational parameters. The Android Application is separated into two parts: the functional component (written in Java), and the graphical component (written in XML). The functional component forms the core of the App. It receives user input and performs all the calculations required. The graphical component, as the name implies, is simply the graphical user interface.

1.1. Background & Theory

The RACM is based on weak backscattering ultrasonic waves, which is mainly due to the high impedance mismatch between the concrete and the cracks and flaws in the medium. The acoustic impedance is positively correlated to the stiffness of the material; therefore, elastic mechanical waves can efficiently be implemented for damage detection. Once the incident wave is excited on the concrete surface, three major mechanical waves of p-waves, s-waves, and r-waves will generate in the propagation direction. The p-wave, also known as compression wave or primary wave, have particle motion parallel with the direction of the propagated wave. The s-wave, also known as the shear wave or secondary wave, have particle motion perpendicular to the propagated wave. The Rayleigh wave, i.e. r-wave, is a kind of surface waves, where the particles have retrograded elliptical motion. The r-waves are propagating along the surface to the direction of the propagating incident wave while the p-wave and s-wave are propagating in the body of the medium [5]. All three wave-particle motions are depicted in Figure 2.

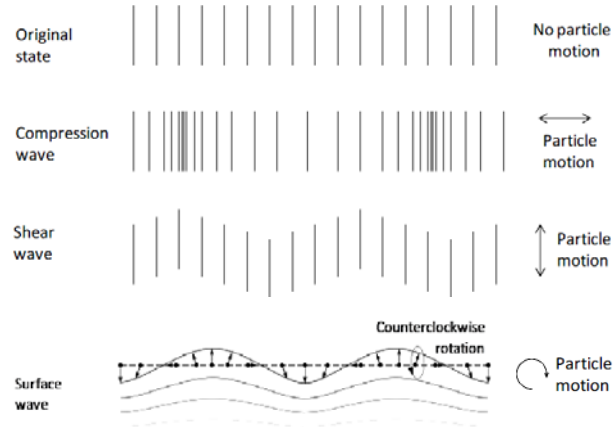


Figure 2. Mechanical waves particle motions.

The velocity of the mechanical waves is the function of the Young modulus, density, and the Poisson's ratio. The derivation of the wave velocities for p-wave, s-wave, and r-wave can be found elsewhere [5][6][7]. The wave's velocities can be obtained as follows

$$C_P = \sqrt{\frac{E(1-\mu)}{(1-\mu)(1-2\mu)\rho}}, \quad (1)$$

$$C_S = \sqrt{\frac{E}{2(1+\mu)\rho}}, \quad (2)$$

$$C_R = C_S \frac{0.87+1.12\mu}{1+\mu}, \quad (3)$$

where, C_P , C_S , and C_R are the p-wave, s-wave, and r-wave velocity respectively, ρ is the density, E is Young's modulus and μ is the Poisson's ratio. Table 1 shows a brief information of the properties of the mechanical waves [8].

Table 1. The mechanical wave's properties [8]

Wave type	Particle motion	Propagation medium	Relative wave speed, $\mu=0.2$	Energy content (%)
P-wave	Parallel to propagation direction	Solid, liquid, or gas body wave	0.61	7
S-wave	Perpendicular to propagation direction	Solid body	1	26
R-wave	Retrograde elliptical	Surface wave	1.09	67

The RACM uses the energy of the incoherent backscattered waves to characterize the level of damage in the concrete. The incoherent backscattered waves are the reflected waves of the incident wave due to the existence of defects, i.e. cracks and voids. The defects can be recognized regardless

of the complexity of internal structures made of inhomogeneous materials. The RACM technique uses a combination of spatial average (SAV), backscatter scans (BS), and low frequencies (LF), which takes advantage of low-frequency ultrasonic waves for inhomogeneous materials that have been traditionally regarded as noise. Figure 3 shows the fundamental concept of the RACM technique. To extract the diffusely scattered field signal B_i from the total wave field that contains coherent pulse content, the averaged signal was subtracted from each of the individual signals within the set,

$$B_i = Bv(t)_i - \frac{1}{N_{path}} \sum_{i=1}^{N_{path}} Bv(t)_i, \quad (4)$$

where, $Bv(t)_i$ is the i^{th} time signal (see Figure 3 for an example backward signals in orange and blue), $\frac{1}{N_{path}} \sum_{i=1}^{N_{path}} Bv(t)_i$ is the overall spatial average $Bv(t)_i$ defined as $\langle Bv(t) \rangle$, and $N_{path} = 9$. Figure 3 shows an example of a backward B_i signal in orange. The average scattered energy, EB_i , expressed in units of V^2 for experimental data, was obtained by integrating the individual scattered signals over a given period of time.

$$EB_i = \frac{1}{t_2 - t_1} \int_{t_1}^{t_2} |B_i(t)|^2 dt. \quad (5)$$

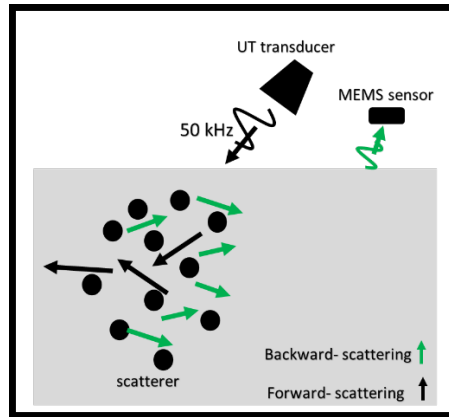


Figure 3. The reflection of ultrasonic energy away from the original direction of propagation, caused by reflection, refraction, and mode conversion from internal inclusions. Causes of signal loss include signal dispersion and scattering “noise”.

To eliminate the effect of inhomogeneity of concrete, which is essentially needed to make the RACM a reference-free method, the backscattered energy was normalized by the energy in the forward propagating wave. The energy of the forward propagating surface wave can be obtained by placing a sensor in front of the ultrasonic transfer which is in the direction of the propagation of the incident wave. The energy of a forward wave is obtained as follows

$$VB_i = \frac{1}{t_4 - t_3} \int_{t_3}^{t_4} |Fv_i(t)|^2 dt. \quad (6)$$

1.2. Instrumentations

1.2.1. Mechanical strain gauge

The expansion measurement of the concrete specimens was carried out using Mayes Instruments Demountable Mechanical Strain Gauge (DEMEC). The DEMEC consists of a digital dial gauge attached to an Invar bar with travel needle of 1 inch. The device has a resolution of 0.001 mm that makes it a strong tool for small-scale expansion measurements. The DEMEC is available upon different sizes of invar bars. The device consists of a fixed conical point, which is mounted at one end of the bar, and a moving conical point on a knife edge pivot at the opposite end. The dial gauge measures the movement of the conical point underneath. The device comes with a reference bar, which is used for calibration. In addition, for sake of accurate measurement, 1 mm drilled stainless steel discs or hexagonal screws are essentially needed to be installed on the specimen's surface. Since the surface of the specimens is subjected to damage, using the stainless steel disks or screws can reduce the margin of error in the measurements. Figure 4 shows the device with the stainless steel disks and a hexagonal bolt. In this research, with respect to the designed specimen size, a 300 mm DEMEC and the hexagonal stainless steel bolts are used.



Figure 4. The Demountable Mechanical Strain Gauge (DEMEC): 300 mm DEMEC (left), 1mm drilled stainless steel disks and bolt (right).

1.2.2. Data Acquisition (DAQ) system

A Data Acquisition (DAQ) system is developed to acquire signals from the sensors and digitalize the analog signal and send the data to a computer. Two different DAQ are used in this research. A 4000 series PicoScope (4824) is used to acquire analog signal obtained from the piezoelectric accelerometer and the developed ultrasonic MEMS sensor. The 4824 PicoScope consists of 8 channels with BNC terminal, 12-bit vertical resolution, and 80 MS/s sampling rate, which assures the quality of the digitalized signals. In addition, a PicoScope TC-08 USB is used for the acquisition of signals from the thermocouples. The DAQ provides 8 channel thermocouple data logger, measurement variation of -270 to 1820 °C, the sampling rate of 10 measurements per second.



Figure 5. DAQ system: PicoScope TC-08 USB for acquisition of the thermocouples signals (left), PicoScope 4842 for acquisition of the accelerometers and the MEMS sensor's signals (right)

1.2.3. Sensors

The model 353B15 piezoelectric accelerometer of PCB Piezotronics is used for the resonant frequency tests of both slabs and prisms. The sensor has the sensitivity of 10mV/g, the measurement range of ± 500 g pk, broadband resolution of 0.005 grms and frequency range of 10000 Hz, which is perfectly suitable for the aforementioned tests. It is noteworthy that a Finite Element Analysis (FEM) of the resonant frequency test was carried out to obtain the required frequency range of the sensor, which is discussed in the finite element resonant frequency analysis section.



Figure 6. Piezoelectric sensor for vibration measurement

An ultrasonic acoustic MEMS microphone SPM0404UD5 is used to equip the RACM developed a handheld device to acquire the ultrasonic signals. The sensor has the sensitivity of -46 to -38 dB, current consumption of 250 μ A across 1.5 to 3.6 volts of supply power. The details of SPM0404UD5 will be uploaded on the database material. In order to use the sensor, a Printed Circuit Board (PCB) is designed and developed to make the MEMS sensor functional. The PCB is designed by PI research team.

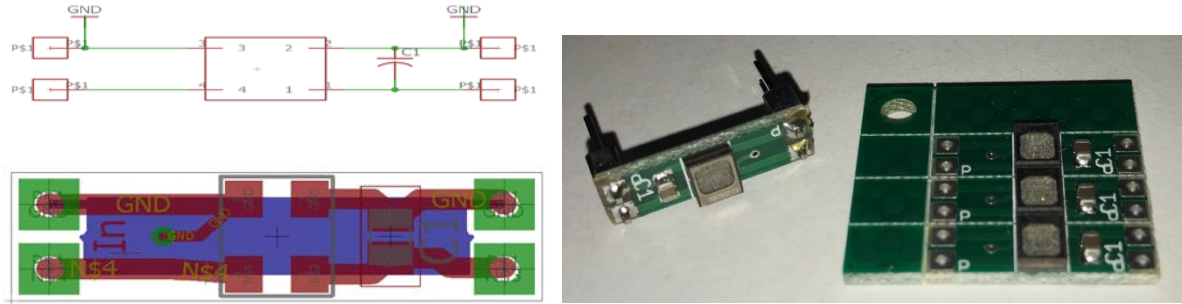


Figure 7. MEMS sensor: schematic and design layout of the MEMS sensor (left), the produced MEMS sensor using SPM0404UD5 microphones (right)

A thermocouple type T was used to measure the specimen's inside temperature. The thermocouple type T has a measurement range of -270 to 370 °C, which is suitable for this Application. The tip of the thermocouple's wires was soldered together to reduce the chance of detachment along the casting or testing.

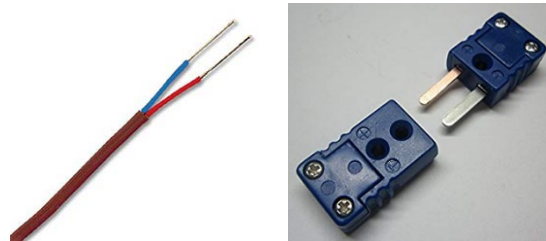


Figure 8. The thermocouple sensors: thermocouple wires (left), thermocouple connectors (right)

1.2.4. Pre-Amplifier

5134B Kistler signal conditioner was used to magnify the signals gain. Type 5134 has four channels of Integrated Electronics Piezoelectric (IEPE) sensors. In addition, it is a microprocessor-controlled coupler that provides DC power and signals to process each channel. A special feature of this type is that with a 0 mA constant current excitation channel setting, the channel acts as an AC coupled voltage amplifier. The Kistler 5134B is able to adjust the gain from 0.5 to 150 which is a perfect match with the selected piezoelectric sensor for a resonant frequency test.



Figure 9. Kistler 5134B signal conditioner

1.2.5. Transmitter

An electrostatics 50 kHz air-launched ultrasonic transducer is used to generate the ultrasonic wave on the concrete specimens. The transmitter has the beam angle of 15° at -6 dB and the range from 6" to 35'. The sensor is able to be triggered internally and externally.

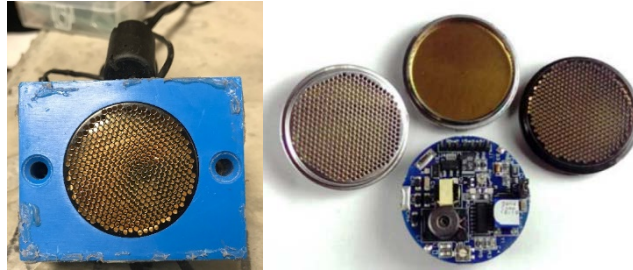


Figure 10. 50 kHz ultrasonic transmitter

1.2.6. Contact 3D tomographic ultrasound (MIRA)

3D tomographic ultrasound (MIRA) is a contact ultrasonic device using 40 transducers, arranged in four columns. Each transducer is able to send and receive ultrasonic waves, resulting in 45 individual transducer pairs per measurement. The transducers excite ultrasonic waves and receive the bounced back signals due to a discontinuity in the medium (i.e. crack in concrete specimens). The wide sensor array technique enables MIRA to provide high-resolution 3D images of the defects using a synthetic aperture focusing technique with combinational sounding (SAFT-C). The method coherently combines pulse-echo measurements to construct a map of the ultrasonic reflectivity of the region being insonified. SAFT takes advantage of both spatial and temporal correlations to improve the quality, i.e. resolution, and the signal-to-noise ratio, of the resultant images [9].

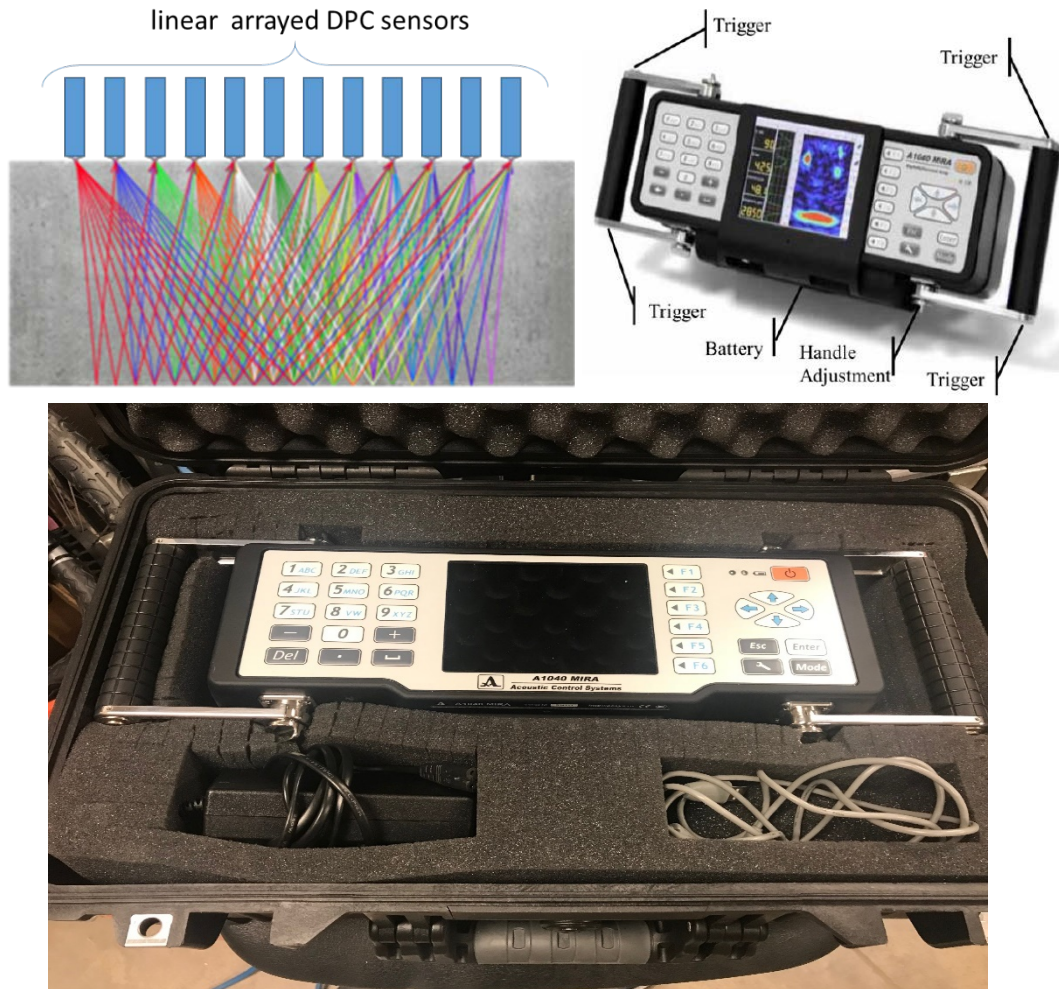


Figure 11. Contact tomography system (MIRA): (left) linear arrayed sensor in MIRA on concrete sample, and (right) 3-D representation of internal defects by MIRA system.

1.3. Device Developments

1.3.1. RACM handheld device development

The RACM handheld structure is designed and developed using the 3D printer. It consists of two lever arms around the adjustable transmitter holder, which hold the MEMS sensors PCB, shown in Figure 12 (top). In order to preclude the sonic waves, two baffles (in front and behind the transmitter) considered for the RACM system with absorbing and diffusing materials. For this purpose, wood was used as a diffusing material and sound barrier rubber foam was used to absorb the sonic waves. The result, provided in the parametric study section, shows that the combination of absorbing and diffusing baffle provides more mechanical waves. Therefore, a baffle including diffusing and absorbing material used in the RACM testing. The distances between the forward and backward MEMS sensors' array were calculated to obtain at least four mechanical waves with no interference of the acoustic wave. Figure 12 (bottom left) shows the schematic of the RACM

configuration with the air-lunch transmitter and the MEMS sensors. The RACM employs the 50 kHz air-lunched ultrasound transmitter to excite an ultrasonic wave into the target medium, i.e. concrete. Inexpensive contactless silicon-based miniature MEMS acoustic sensors were used and located at 1 cm above the surface to record the forward and backscattering waves, traveling in the concrete specimens. The MEMS sensors are designed, tested and implemented at The University of Texas at Arlington. For the forward measurement, two layers of sensors were placed, i.e. sensors #8 and #9, to acquire forward propagated a mechanical wave's signals. The number of 8 MEMS sensors were placed in three layers behind the ultrasonic transmitter to acquire the backscattering signals. However, since the DAQ is limited to 8 channels, and one channel was assigned to the transmitter, MEMS sensors #5 and #7 were put aside of the acquisition. Figure 12 (bottom left) shows the configuration of a MEMS sensor on the designed PCB, where every three sensors are powered by series of 1.3V batteries (total of 2.6V). The BNC terminal was used as the output of the MEMS sensors. This terminal was chosen to be in conformity with the DAQ output.

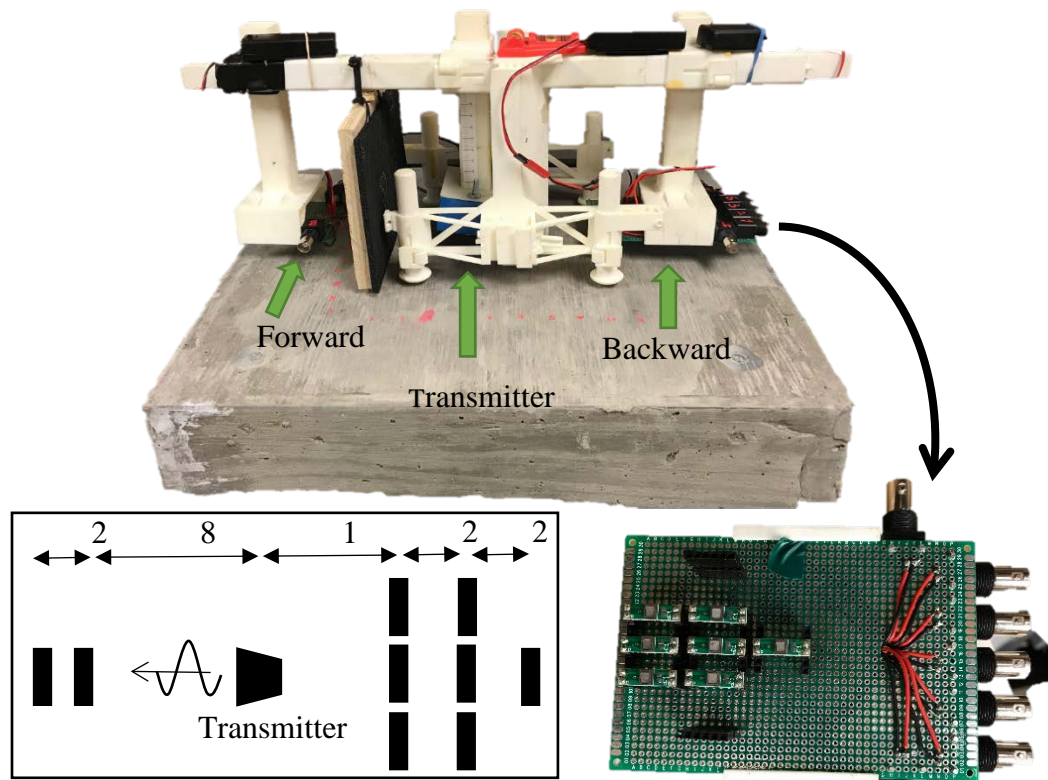


Figure 12. RACM handheld device: the RACM handheld device configuration (top), the schematic of the sensors' configuration in the RACM handheld device (bottom left), the developed PCB for backward MEMS sensors with BNC cable output (bottom right)

1.3.2. Freeze and Thaw Machine

In order to make degraded concrete specimen exposed to the F&T cycles, an automatic F&T machine has been designed and developed at the University of Texas at Arlington, this machine is able to bring the center of the concrete specimen down to -18 °C and increases it up to 30°C.

However, in this research, the device was set to heat up the concrete specimens to 4°C. The machine consists of a stainless steel freezer, control timer plugs, and heating elements. The number of two heating elements were attached to an aluminum tray. In order to attach the heating elements to the trays, L-shape aluminum components were welded on both sides of the trays to hold the heating elements tight to the tray's wall. The heating elements were tightly attached using screws and nuts through the L-shape components as shown in Figure 13 (right). The control timer plugs are a programmable smart plug, which can be programmed to connect or disconnect the electrical current at any predefined time. Three plugs were used in this research, where one plug was assigned to the freezer, and two were allocated for the heating elements. The reason for using two plugs for the heating elements was the maximum allowable current of the laboratory's electrical circuit, which was limited to 15A and the total current of the heating elements was above 15A. Therefore, two plugs were used in different outlet circuits to prevent wire's overheat and fuse jumps. The timers were set such that once the heating elements are working (thawing cycle) the freezer turns off and while the freezer is working (freezing cycles) the plugs cut off the electric power. The freezing and thawing duration time was determined through the parametric study provided in the parametric study section.

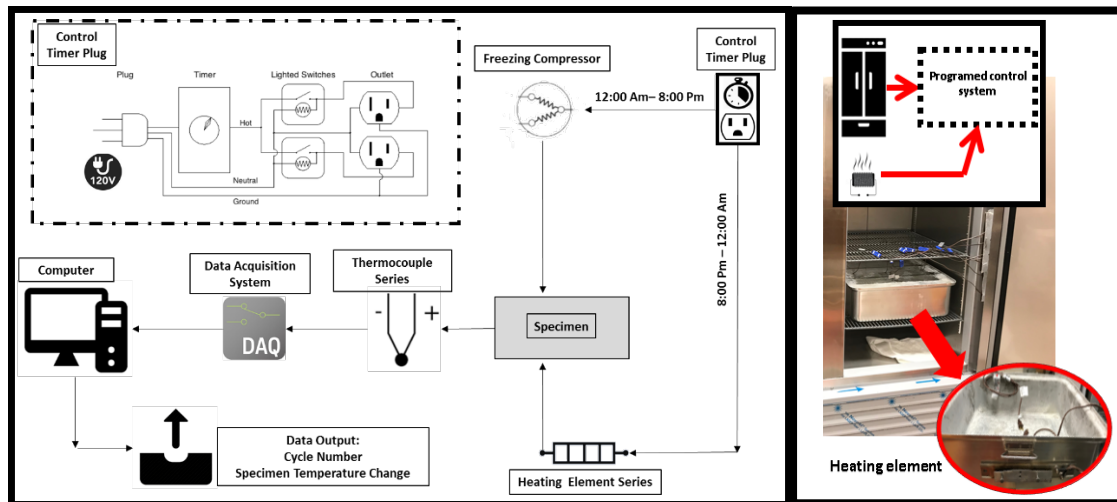


Figure 13. Freeze and thaw machine: the schematic of the F&T machine (left), and the freezer, heating elements and the tray (right).

2. Numerical Analyses

2.1. Finite element resonant frequency analysis

An Eigen-value analysis has been carried out using finite element simulation to obtain the first flexural resonant frequency. Prism elements were used to verify the FEM model and after the optimization of the FEM analysis using the inverse analysis, the first flexural mode of the slab specimens was obtained. This study gives the vision to the PI to choose the correct frequency peak during the resonant frequency test. Figure 14 (right) illustrates the Eigenvalue analysis simulation of the prism element where the transverse flexural mode's frequency is in conformity with the resonant frequency test of the prism element depicted in Figure 14 (left).

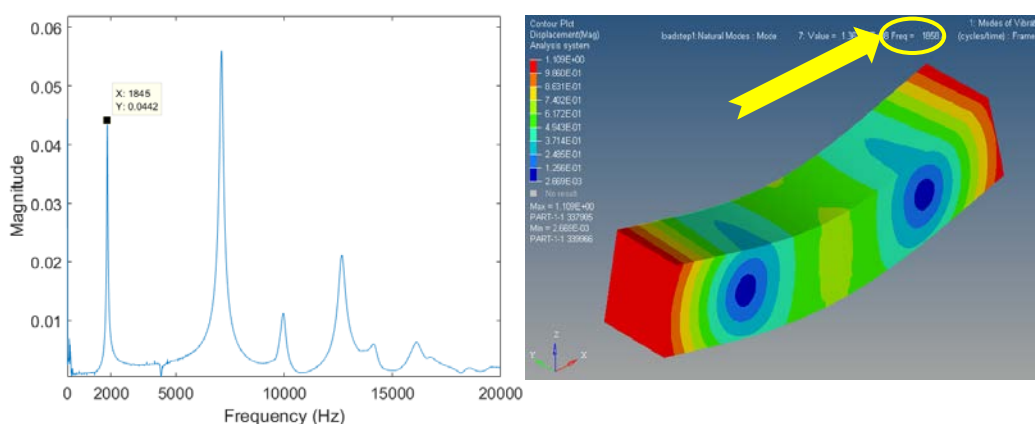


Figure 14. Resonant frequency result of prism specimen: the resonant frequency test (left), and the FEM simulation for Eigen-value analysis (right).

Using the same material properties for the slab specimen in the Eigen-value FEM analysis ended up with the frequency of the flexural mode, which determines the correct peak to be read in the resonant frequency test. Figure 15 shows the result for the Eigen-value analysis and the resonant frequency test result of the slab specimens.

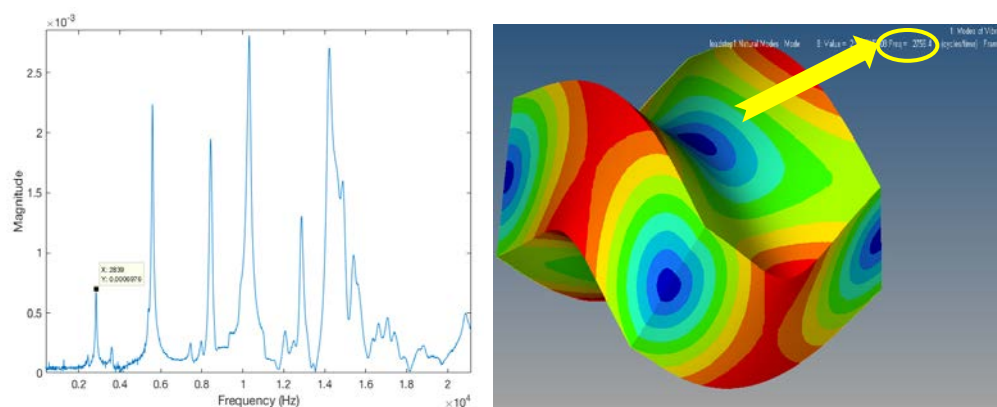


Figure 15. Resonant frequency result of slab specimen: the resonant frequency test (left), and the FEM simulation for Eigen-value analysis (right).

2.2. Finite element 2D random shape of aggregate model using image processing and convex combination theory

Ultrasonic non-destructive testing (UNDT) is used for detecting and locating damage in concrete structures such as bridge decks and pavement. There are even advanced UNDT methods such as the incoherent backscattering approach that is one of the effective methods to characterize the distributed microcracks in the homogenous concrete infrastructures sensitively. However, the shape and orientation of the aggregates play an integral role in wave reflection, refraction, and mode conversion from internal inclusions. Moreover, the microcracks also tend to go deeply into the interfacial transition zone. The numerical simulation of such advanced UNDT helps to understand and predict this physical phenomenon but requires the existence of realistic shaped coarse aggregates to understand the wave propagation phenomenon accurately. Therefore, this study presents a 2D mesoscale heterogeneous model for concrete in which the coarse aggregate shape and location are randomly generated and placed in the mortar matrix to construct a random-shaped aggregate model. To achieve this goal, a morphological study was carried out on a thousand of aggregates using the image processing technique to characterize their shapes and categorize them into the three major classes: round, crushed, and needle shape aggregates. By implementing statistical analysis and the convex combination theory, the randomly generated aggregate model was developed for each class, which is derived from the real aggregate image using plain formulation. Consequently, by using the obtained parameters, a 2D convex combination theory based random shape aggregate model (CCT- RSAM) was generated which can be used in the construction of the random aggregate structures.

2.2.1. Methodology

The proposed mesoscale 2D CCT-RASM model for concrete contains randomly-generated aggregate shapes from RSAM and randomly distributed coarse aggregate in cement paste medium. The approach considers more realistic 2D aggregate shapes which includes all three groups of aggregates, which exist in the concrete cross section. Concrete samples were prepared, and cut into slices using a concrete saw machine; then, the sample cross-section pictures were taken with a high-resolution digital camera, and through the developed image processing algorithm images, the aggregates were detected and stored as binary images. This technique enabled the authors to obtain an accurate shape of each aggregate so that all the aggregates can be categorized into three groups as a profile. Moreover, the shape profile makes this aggregates characterization possible. To eliminate the effect of the different orientations of similar aggregates in the signature curve, the cross-correlation and Hausdorff distance methods were used to detect similarly shaped aggregates. Afterwards, through convex combination theory (CCT), the numerical models were obtained for each group, which generates random shape coarse aggregate. Also, the statistical analysis was carried out to obtain each group's distribution along the concrete cross section.

2.2.1.1. Cross-Correlation and the Hausdorff Distance Method

This method is to estimate the correlation between two random sequences [10]. The cross-correlation between two stationary random processes of x_n and y_n is given by:

$$R_{xy}(m) = E\{x_{n+m} y_n^*\} = E\{x_n y_{n-m}^*\}, \quad (7)$$

where $-\infty < n < \infty$, E is the expected value operator, and the asterisk is the complex conjugation. In this research, the aggregate's similarity check through the cross-correlation method is also verified with the Hausdorff distance method which is proposed to determine the degree of resemblance between two objects [11]. The Hausdorff distance method takes one point from the first object and calculates the distance with all the other points on the second object and chooses the minimum value. This procedure will be repeated for every single point on the first object. The maximum of the minimum distances is determining the level of resemblance between two objects with the lower value representing the most resemblance between them. Obviously, the zero value means both objects are geometrically identical. The Hausdorff is defined as:

$$H(A, B) = \max(h(A, B), h(B, A)), \quad (8)$$

where,

$$h(A, B) = \max_{a \in A} \min_{b \in B} \|a - b\|. \quad (9)$$

The function $h(A, B)$ is the direct Hausdorff distance from the aggregate A to aggregate B. It identifies the nearest distance for point a on the aggregate A to its neighbor on aggregate B using the given norm $\| \cdot \|$. The Hausdorff distance methods verified the results of the cross-correlation method which assures the credibility of the aggregate similarity check. Figure 16 (a) shows the cross-correlation method where the proper rotation angle is found, and the aggregate is rotated so that the similar aggregates lie in the same orientation. Figure 16 (b) shows the Hausdorff distance method between two objects.

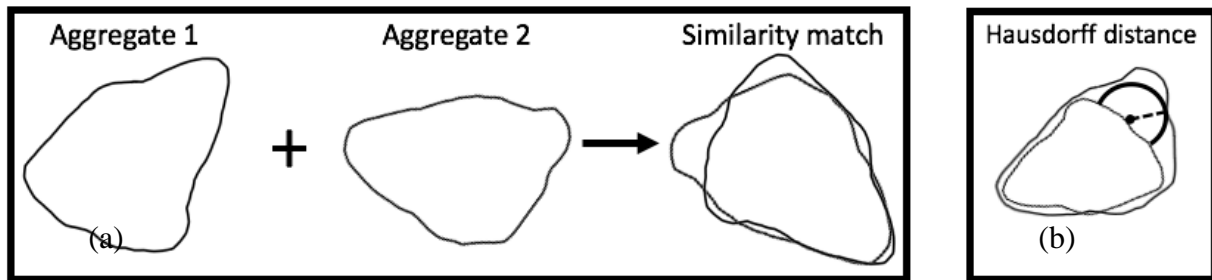


Figure 16. Procedure of the aggregate similarity check using cross-correlation and Hausdorff distance method by detecting the the best rotation angle: (a) Cross correlation method and (b) Hausdorff distance method

2.2.1.2. Convex Combination Theory

The convex combination is a linear combination of points with non-negative coefficients where for a finite number of points the convex combination is described as:

$$Y = C_1x_1 + C_2x_2 + \dots + C_nx_n. \quad (10)$$

In this equation, the C parameters are the coefficients, where, $C_1 + C_2 + \dots + C_n = 1$. To generate random aggregates among the selected aggregates, the coefficients should be selected randomly. Therefore, to keep the summation of the coefficients equal to 1, the following algorithm is used:

$$C_1 = \text{random}([0, 1])$$
$$C_n = \text{random}\left(\left[0, 1 - \sum_{i=1}^{n-1} C_i\right]\right). \quad (11)$$

2.2.2. Procedure of random aggregate generation

The concrete samples were cast with the Portland cement Type I, fly ash Class C, limestone aggregate grading with a granular diameter from 9.525 to 38.1 mm (0.375 to 1.5 in.) and sand with a particle size range from 0.076 to 4.75 mm (0.003 to 0.187 in.). For the concrete mix, we composed a mixture with 650 lbs./cu.yd. of type I cement and a 0.364 water-binder ratio. A well-graded sand and crushed limestone coarse aggregates with the maximum diameter of $\frac{3}{4}$ were used. The mixture proportions by mass were 1:0.38:2.84:1.72 (binder: water: fine aggregate: coarse aggregate). The Class C fly ash was used in the mix design to increase the workability of the concrete. Moreover, for the sake of higher quality of image processing, a charcoal cement color was added to the batch to provide a higher contrast between the aggregates and cement. The samples were cured for seven days in a moisture curing room. The specimen size was selected in conformity with the ASTM C 78 standard specifying a 6 x 6 x 20 in the beam. The beams were cut with 25.4 mm (1 in.) width slices, and each side of the slice was polished to eliminate saw machine traces from the surface in Figure 17 (a & b). Moreover, the surfaces were rinsed to wipe off the dust and mud stemming from the saw and polishing procedure to increase the accuracy of aggregate edge detection.

2.2.2.1. Digital image processing (DIP) of concrete cross section

The digital image processing (DIP) algorithm is developed for processing of the concrete cross section's image and obtaining the accurate aggregate shape profile. It requires a high-quality binary digital image. Figure 18 shows the image processing procedure, where the binary aggregate image is obtained from the cross-section of the specimen. For this purpose, initially, the images were converted to a grayscale image, and later they were converted to a binary image for the sake of image registration (Figure 18 (b)). In the image processing, the logical value of 1 is imposed on the pixels in the grayscale image with an intensity above the specified binary threshold; then, 0 is

imposed for the lower intensity value. Therefore, in the binary image, the paste is shown with black as the logical value of 0, and aggregates are white as the logical value of 1. To eliminate noises, undesired small particles (e.g., large sand particles), the area limitation is imposed in the DIP procedure which rules out detected objects less than a specified area value. Also, the object filler algorithm, based on morphological reconstruction [12], is used to fill the objects which did not impeccably convert to binary. By implementing the image registration algorithm, the aggregates were labeled and stored as separate images. The aggregate sizes were normalized for ease of comparison so that the returned aggregate image had a maximum radius of 1. Once the aggregates were normalized, the geometric centroid of the aggregates was obtained, which is required for aggregate translation and rotation. To avoid the conversion or rotation error, the aggregates location was adjusted so that the centroid of the aggregates laid on the center of the image (Figure 18(d)); otherwise, in those procedures the operations will be done in respect to the center of the image not the center of the aggregate, which is not favorable. In the next step, the aggregate edges were detected using the Sobel approximation method which returns the edges of those aggregates, where the gradient of the image is maximum. In this application, the Sobel approximation method was chosen since this method, unlike the other methods such as the Laplacian of Gaussian, Canny approximation, etc., returned the same resolution of the aggregate image and provides more accuracy. In the last step, the signature curve of the aggregates was obtained by the conversion of the polar coordinates of the aggregates to the Cartesian coordinate system illustrated in Figure 18 (e). By implementing this technique for the 40 slices of real concrete specimens, 1072 coarse aggregates were obtained and taken under study to analyze their shape and characteristics.

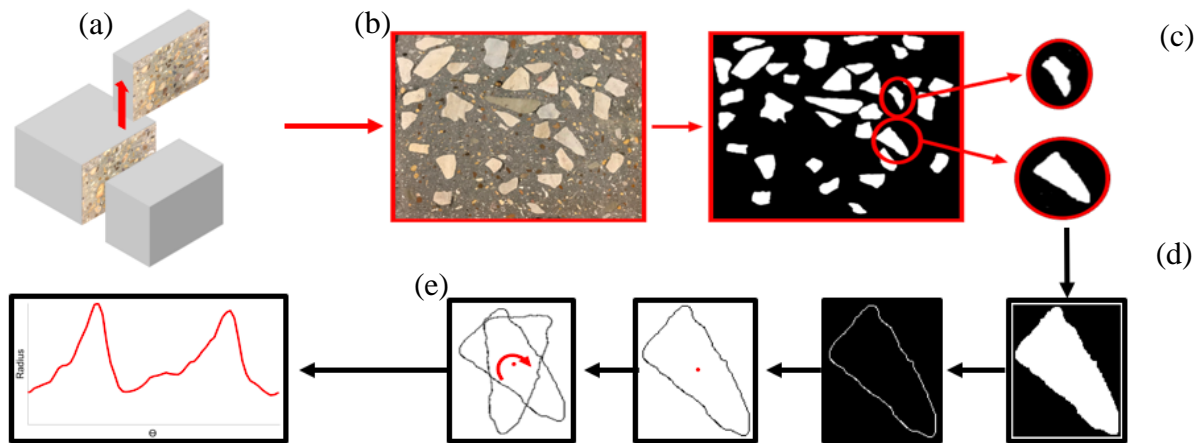


Figure 17. Digital image processing procedure: (a) Sample preparation, (b) image digitalization, (c) image registration, (d) edge detection using Sobel approximation and centroid determination for the rotation procedure, and (e) coordinate conversion from polar to Cartesian.

2.2.2.2. Morphology-Based Signature Curve and Classification of Model using Aggregate Dispersion Statistical Analysis

From these images using the DIP technique elaborated above, the coordinates of the aggregate edges were obtained and later converted to the polar coordinate system. The signature curve of the aggregates was plotted with polar radius versus the polar angle of the aggregate. Figure 18 (b) shows the signature curve of an aggregate illustrated in Figure 18 (a) which depicts the alteration of the aggregate radius along the aggregate edges at different angles. It can be implied from the curves that the peaks and troughs are the convexity and concavity of the aggregates. The greater difference between the highest peak of the radius value and lowest trough represents the rate of aggregate elongation (e.g., needle-shaped aggregates, crushed, etc.); conversely, the lower value presents the roundness of the aggregates (i.e., gravel). Moreover, the repetition of the low amplitude peaks and troughs represents more irregular aggregates (i.e., crushed aggregate).

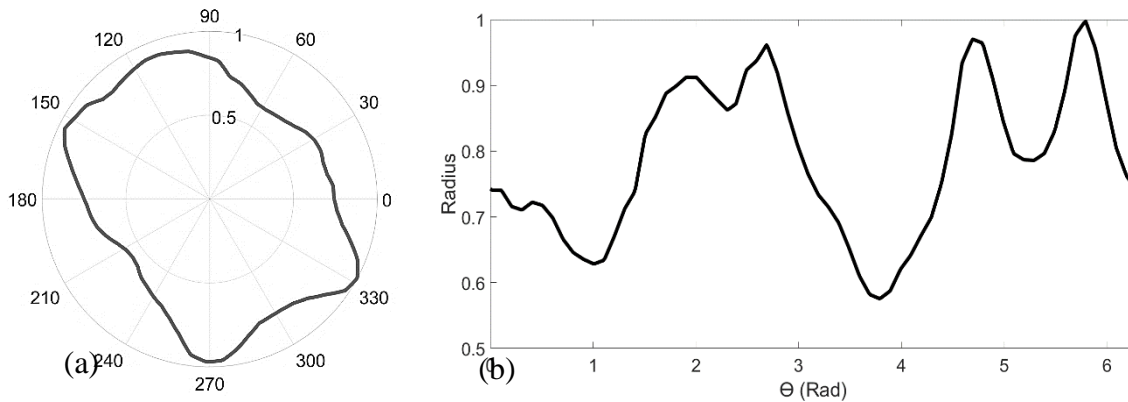


Figure 18. Presentation of the generated aggregate in a polar curve (a) and its signature curve (b).

Once the signature curve conversion is carried out for each aggregate and their aspect ratios have been calculated, the aggregates were plotted based on their aspect ratio and their appearance number in the image registration procedure. Figure 19 shows the aspect ratio of each aggregate which enables us to categorize the aggregates based on their shapes into three classes of round, crushed, and needle shape aggregates. Once the classification of the aggregates has been carried out, the signature curve of each group of aggregates was plotted. It is crucial note that since the aggregates are random in shape, orientation, and dispersion in the cement medium, it is highly possible for two similar shaped aggregates to exist with a different orientation, where they cannot be identified in the signature curve due to the phase change. A two-step process is required to avoid the phase change issue: 1) equalization of the aggregates data points and 2) adjustment of the aggregate orientation. A direct comparison is not possible, due to the different number of data points in each aggregate. Moreover, for ease in similarity checking, the number of data points should be 360 points before rotating the aggregate for every one degree and checking the similarity. Therefore, an appropriate interpolation method can equalize the data points of each aggregate as an equalization process. To this end, among the different types of interpolation methods, linear interpolation provides a more accurate shape. While, the other methods including the spline

method, can deviate the shape of the aggregate. To find the best rotation angle for eliminating the orientation effect of the similar aggregates, the cross-correlation method is used, which compares all the aggregates with the reference aggregate and returns the angle, which provides the highest similarity to the reference aggregate.

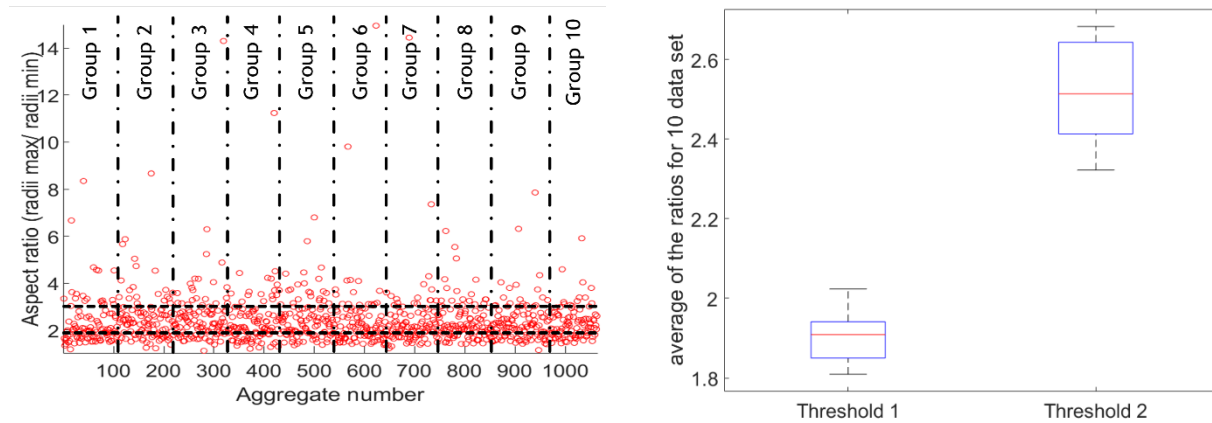


Figure 19. Statistical studies on the aggregates: to determine type based on the aspect ratio (left) and distribution of the thresholds from 10 sets (right)

Figure 19 (a) shows the aggregate distribution based on the order of their appearance and their aspect ratio where the aspect ratio of the aggregates is expressed as radii max/ radii min. The ten sets of aggregate samples were chosen randomly to find the threshold and check the aggregate distribution of each group as illustrated in Figure 19 (a). To find the threshold between the groups, the lower one-third of the aggregate number was selected as the round aggregates, so that the aspect ratio of the last aggregate in the lower one-third set is defined as the threshold between the round aggregate group and the crushed aggregate group. Likewise, the middle one-third set of the aggregates was selected as the crushed aggregate group, and the last aggregate's aspect ratio in this set was selected as the threshold between the crushed aggregate group and the needle shape aggregate group. The same procedure was carried out for the other nine sample sets, and their distribution has been determined uniform through the fit test. Therefore, the borderline between the three groups was determined by averaging the thresholds of all ten sets. Figure 19 (b) shows the boxplot of the thresholds where the values of the 1.891 and 2.482 are the threshold means for the round, crushed and needle shape aggregates, respectively. These values were then chosen as the main threshold for the aggregate classification boundaries.

2.2.2.3. Construction of Random Shape Aggregate Model Formula Using Convex Combination Coefficients

To generate a formula that can represent all the data sets for all the aggregates in each group, the regression analysis cannot be useful. This is because the variance of the data is too high, which means the regression curve cannot be representative of all curves. Moreover, the fitted curve is only presenting the average of all aggregates which is not favorable. Thus, among all the aggregates in each group, the most repeated shapes and the least repeated shapes must be found to generate RSAM. Therefore, once the aggregates are sorted through the cross-correlation method

and categorized into the three sections, statistical analysis was carried out for each group at points 0, 2.3, 4 and 5.5 radians, where the major peaks occur in the signature curves (Figure 20); then, we can obtain the distribution of the aggregate's diameter at those points. The goodness of the fit test shows the distribution of the data for the diameter in all three cases in the four points is lognormal. The mean and standard deviation of the data sets at each point is calculated, and the aggregates with the diameter within the 95 % level of confidence at all 4 points are selected as the most repeated shapes. The same procedure is carried out for the least repeated shapes where the diameter of the aggregates relies on a 5% level of confidence in the all 4 points, which means the aggregates with the diameter within this range, at those points, are repeating the least. For both cases, the common aggregates, which lay within the ranges in all four points (i.e., 0, 2.3, 4, 5.5 radians), are selected as the reference aggregates for the random aggregate generation procedure. As the result 6, 7, and 8 reference aggregates were detected for the crushed, round and needle-shaped of the aggregates groups, respectively. Afterward, from the signature curves of these aggregates, the random generation can be carried out by the implementation of the convex combination theory, which encompasses the least and the most repeated aggregate profile. Therefore, any generated aggregate model through these curves can be representative of the other aggregates in each group. In order to regenerate the reference aggregates out of the pictured aggregates, several curve fittings were examined among spline, polynomials, Fourier, and Gaussian series. The summation of sin-series obtained the best fit for the curves. The summation of the sine series is described as follows:

$$Y = b_1 \sin(b_2x + b_3) + \dots + b_{n-2} \sin(b_{n-1}x + b_n), \quad (12)$$

where x is the polar angle and varies from 0 to 2π and b_i for $i = 1:n$, which are the coefficients of the fitted curve for each aggregate and are provided for each group (i.e. round, crushed, and needle-shaped). Therefore, the aggregates of each group can be reconstructed through the substitution of the provided coefficients in the tables into equation (12). In order to generate the random aggregates of each group, the convex combination coefficients must be randomly generated using equation (11) and placed into equation (12). Notably, the convex combination coefficients give weight to each aggregate shape; consequently, the higher value of the coefficient of one aggregate implies that the generated aggregate is more characterized by that aggregate.

The fitted curve coefficients of round crushed and needle shapes aggregate are introduced on Appendix A.

2.2.3. Results and discussions

2.2.3.1. RSAM Results

The statistical analysis of the aggregate classifications shows that variations in the needle-shaped aggregate aspect ratios are significantly higher than the crushed and round aggregates. Figure 21(a) depicts the box plot of the aggregate aspect ratio dispersion for each group, where the goodness of fit test showed that the distributions are uniform. However, it is noteworthy that the needle shape aggregate group includes a high range of aspect ratios, where less than one percent of aggregates in this group has a very large aspect ratio and must to be considered as outlier data. Otherwise, no distribution function can represent the aggregate distribution. Figure 21(b) shows the curve fitting of an aggregate signature curve with the sine series. Among the many different series, the summation of sines ended up with the best fitting result, while a low amount of discrepancy exists between the fitted curve and the aggregate signature curve. This discrepancy eliminates the very small ripples on the aggregate edges. However, the small ripples on the aggregate edges are negligible, since their size are significantly smaller than the finest mesh size in the FE analysis of such a structure size, and therefore, do not play an integral role in the aggregate morphology. Implementation of these methods led to the generated aggregates for round, crushed, and needle-shaped aggregates illustrated in Figure 22. The generated aggregates include convexity, concavity and most of the attributes of real aggregate morphology.

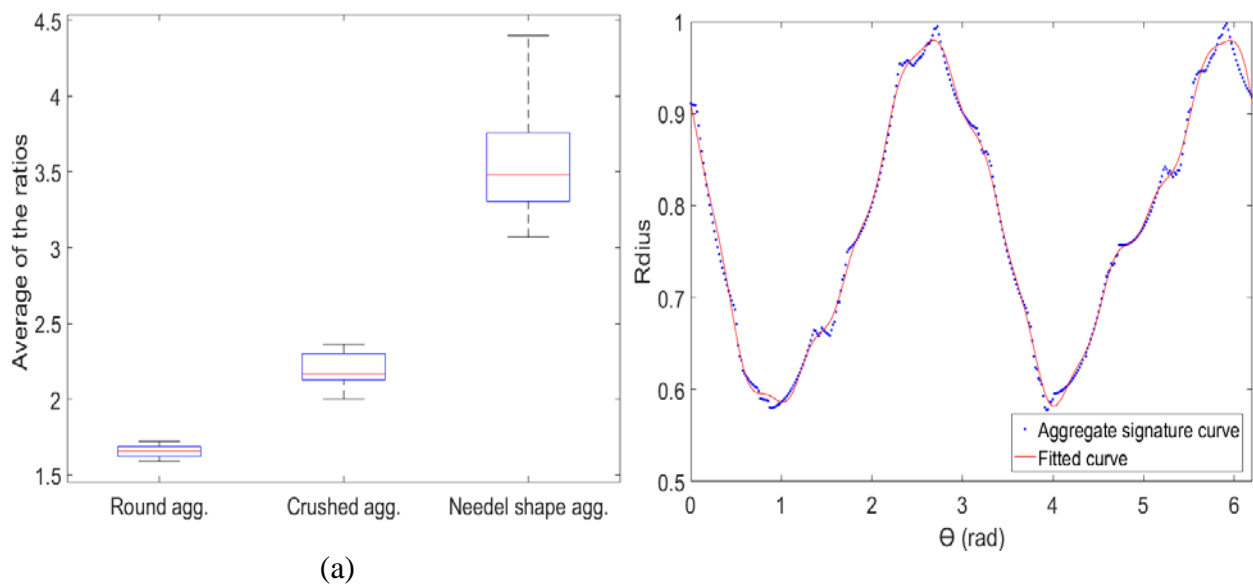


Figure 20. Aggregate analysis of distribution of the aggregates in the groups (left) and curve fitting for the aggregate signature curve (right)

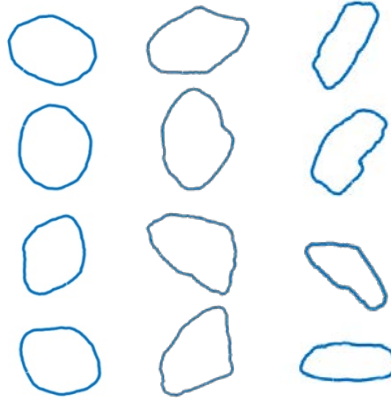


Figure 21. Normalized randomly generated aggregates for the round (left column), crushed (middle column), and needle shape (right column), where the largest diameter of aggregates is limited to 1.

Eventually, by the implementation of modified take and place method, the aggregates can be placed into the sample domain to construct a 2D RAS. The main advantage of this model is the accuracy of the generated aggregate shapes which are derived directly from the most repeated aggregate shape among 1000 aggregate images. Moreover, the generated aggregates contain edge ripples that the methods above were unable to make. Notably, the higher accuracy of the aggregate shape provides a more realistic ultrasonic wave reflection, refraction and mode conversion.

2.2.3.2. The Assessment of the Aggregate Surface Effect on the Wave Reflection

The proposed aggregate model is based on the convex combination of the most and the least repeated aggregates among the statistical population of around 1000 samples, where the generated shapes represent the most realistic shaped aggregates. To verify the validity and precision of the generated aggregates in wave propagation application, an arbitrary concrete cross-section image, has been chosen as a comparison sample. Figure 23 shows the binary image of a concrete cross, taken by Gautam et al. [13], where after the aggregate classification determination, for an instance, a round shaped aggregate was randomly chosen as the reference aggregate and was resized, so that the maximum diameter of the aggregate has the value of 1cm. Thereafter, the aggregate was taken into the FE analysis and subjected to the ultrasonic wave propagation. The practical 50 kHz mechanical wave for concrete [32, 33] was generated and transmitted toward the aggregates, and the reflected signal was collected. In this study, three aggregate models were compared with the reference aggregates. A conventional circle model, hexagonal model and proposed randomly generated round aggregate model. However, for the RSAM, the aggregate and the reference aggregate were analyzed by the cross-correlation Hausdorff distance method to assure the aggregates orientation were in the same direction. Thereafter, the backscattering energy of the transmitted waves from the reference aggregate was calculated and compared to obtain the similarity of the backscattering waves from all types of the aggregates. For this analysis, Young's modulus, density, and the Poisson ratio of the aggregates were considered to be 2.3×10^6 kg/mm², 55.5 GPa, and 0.16 respectively (22). Likewise, the values of 2.6×10^6 (kg/mm²), 35.5 GPa, and 0.22 are chosen for the material properties of the mortar. To acquire an acceptable resolution and prevent the quantization error, the mesh size l_e and the time increment Δt were determined based

on the frequency and the wave speed of the transmitted mechanical wave. The 50 kHz mechanical wave has a wavelength of 44 mm; therefore, the mesh size of 1 mm assures that at least 20 elements can participate to express the wavelength. Likewise, the 1 μs time increment provides 20 data points since the wave's period is 200 ms ($T=1/f$). Therefore, the wave cannot propagate through a one-time increment. To calculate the backscattering energy, at the first step the backscattering signal must be detected. Therefore, the FE analysis was carried out with no aggregates so that no wave reflection due to the aggregate can occur. Figure 24 shows the acquired signal, where the only discrepancy between the aggregate models and the solid model, i.e., the model with no aggregate, is on the coherent backscattering wave stemming from the P-wave. In the last step, the backscattering energy of the reflected wave is calculated through the calculation of the area, under the squared signal:

$$E = \int_{t_1}^{t_2} S^2 dt, \quad (13)$$

where, the E is the energy of the backscattered wave, and S is the signal within the times t_1 and t_2 .

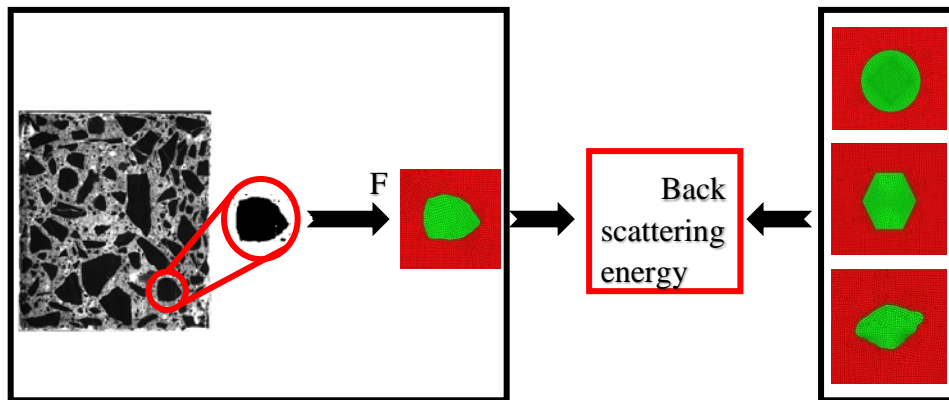


Figure 22. The selection of an arbitrary aggregate as a reference from other studies [13] and conveying the aggregate into a FE analysis model to compare with the three main aggregate models: Circle, hexagonal, and the proposed random shape aggregate.

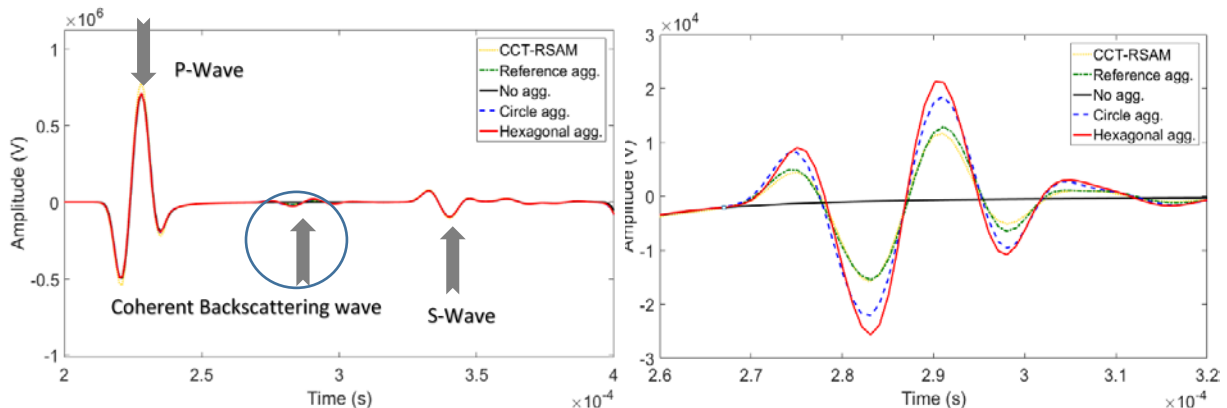


Figure 23. Time domain signal (a) Ultrasonic wave propagation signal from the FE analysis for no aggregate, reference, CCT-RSAM, circle, and hexagonal aggregates and (b) zoomed in the plot in the circle from the left figure

The FE analysis of the generated aggregates and their comparison with the reference aggregates enabled the authors to obtain the backscattering energy of stemming from the existence of the aggregate in the concrete medium (Figure 24). The result showed that, although the generated aggregate is not the same as the reference aggregates, since the generated aggregate's characteristic is based on the most and the least repeated aggregates in a statistical population, the discrepancy of the energy level of both the reference and the CCT-RSAM are less than 3% which assures the credibility of the proposed aggregate method.

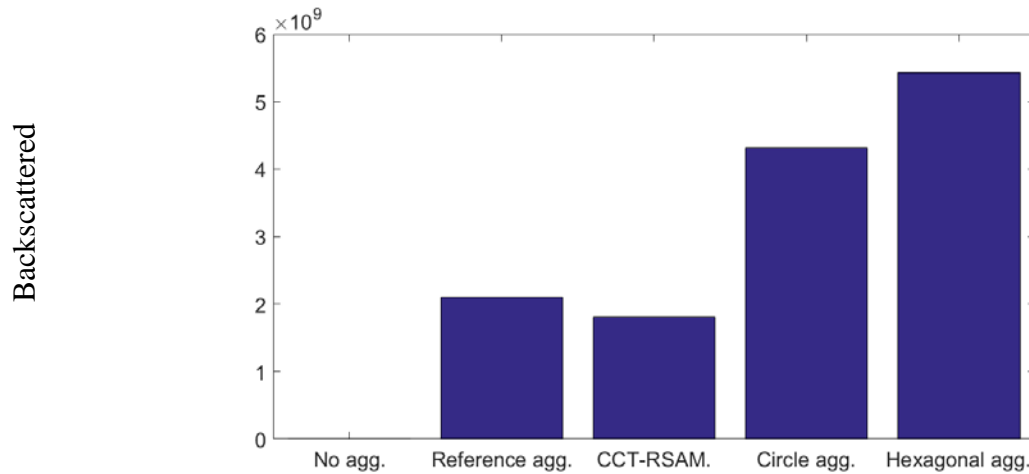


Figure 24. The backscattering energy of the reference, CCT-RSAM, circle, and hexagonal aggregates

3. Specimen Preparation and Parametric study

3.1. Specimens

The concrete specimens used in this study were designed and fabricated in Civil Engineering Laboratory Building (CELB) at the University of Texas at Arlington. The number of five slabs and two prisms were considered in this study; three slabs for the main tests, one slab for F&T parametric study, one as a control specimen, and two prisms for concrete material testing including one testing and one control specimen. The slabs size were designed according to the freezer's entrance span (which was limited to 22 in.) with consideration of enough space for the tray and the heating elements. Also, the main consideration was given to the minimum allowable distance for the RACM testing to acquire at least three mechanical waves, prior to the interference of the reflected mechanical waves, stemming from the specimen's boundaries. By the initial assumption of a specimen with the size of 40 cm x 40 cm x 15.2 cm (16 in. x 16 in. x 6 in.), and consideration

of the r-wave velocity of 2200 m/s, and the safe distance of 10 cm, the wave's time traveling of $1.36e-4$ can be obtained using velocity-distance relationship,

$$V = \frac{d}{t}, \quad (14)$$

3.2. Concrete Designs

Table 2 shows the designed specimen sizes for slabs and prisms specimens. Since the purpose of these samples is to be degraded and the damage volume of the specimens be detected by RACM, the concrete mix design was prepared for the water-cement ratio of 0.53 as shown in Table 3.

Table 2. Specimens' size

Specimen Name	Size (cm.)	Description
Slab	FT1	40 x 40 x 15.2
	FT2	40 x 40 x 15.2
	FT3	40 x 40 x 15.2
	Control	40 x 40 x 15.2
	TC Control	40 x 40 x 15.2
Prism	PT	40 x 8 x 8
	P Control	40 x 8 x 8

Table 3. Concrete mix design

Material	Weight Ratio
Sand (lb/CY)	0.330008068
Aggregate (lb/CY)	0.462803183
Cement (lb/CY)	0.134826725
Super P (12/CY)	0.000010000
W (lb/CY)	0.072352023
Total	1

The molds were fabricated with plywood and the expansion measurement's bolts were installed at the 300 mm spacing, i.e. according to the DEMEC gauge length, on the bottom (top surface of the specimens) and side surfaces of the molds. A thermocouple wire was installed on all slabs at a wet stage of concrete casting at 1 cm depth from one of the sides, shown in Figure 25. For the TC Control slab, seven thermocouple sensor was installed at 1, 7, 14 cm depth to monitor the temperature difference of the specimens at a different time. The thermocouple's positions are depicted in Figure 26. The specimens were cast in different batches since the mixer machine's capacity was not sufficed for casting all specimens at one time. Then, they were placed in a curing room at the CELB, with the humidity of 100% at a temperature of 30 °C and cured for 14 days. Thereafter, the specimens were measured for size and weight and the density of each specimen was calculated and reported in Table 4.

Table 4. Specimens' physical properties after casting

Specimen Name	Measured Size (cm.)	Weight (lb.)	Density
Slab	FT1	40.8 x 41.2 x 15.2	130.44
	FT2	40.3 x 40.4 x 14.5	123.62
	FT3	40.7 x 41 x 14.8	125.5
	Control	40.6 x 41.7 x 14.9	129.96
	TC Control	41 x 40.3 x 15.1	130.44
Prism	PT	40.3 x 8.3 x 7.9	14.52
	P Control	40.3 x 8.5 x 8	15.08

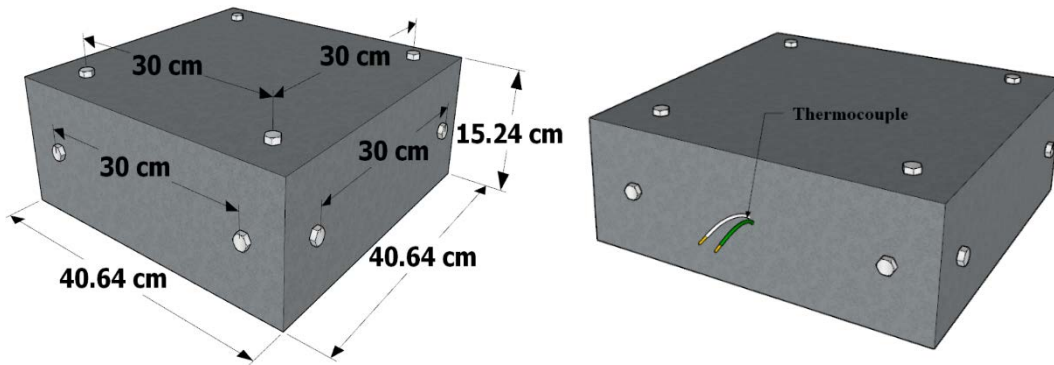
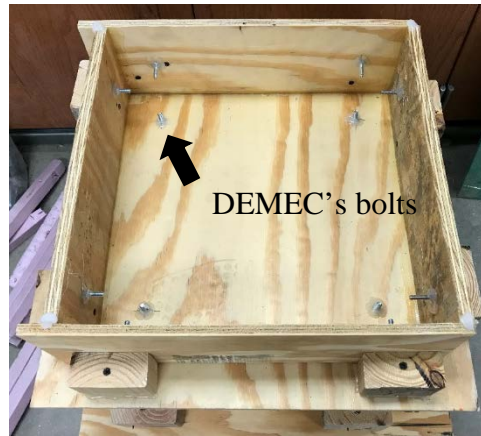


Figure 25. Sample preparation: the mold preparation (top), specimens actual size (bottom left), and the thermocouple location for slabs, FT1, FT2, FT3, and control (bottom right)

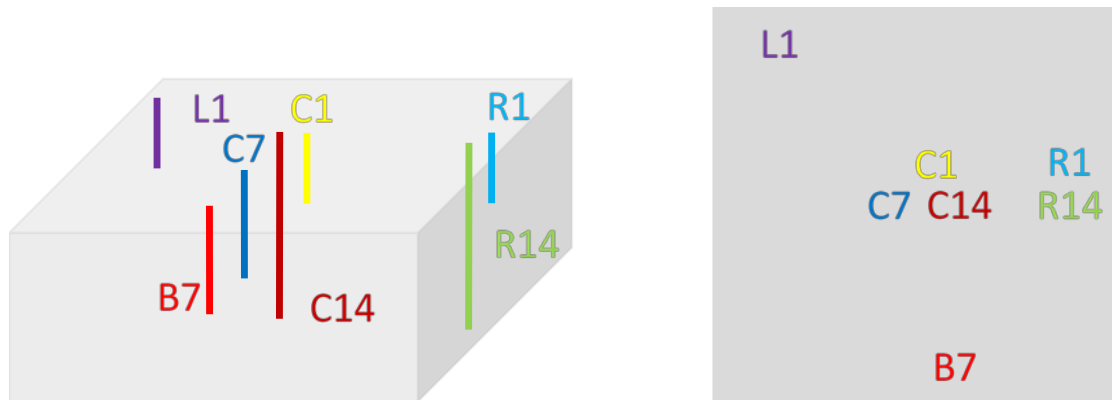


Figure 26. Thermocouple's positions for the TC Control specimen: the 3D view of the location of thermocouples at 1, 7, and 14 cm deep inside the specimen (left), and top view of the thermocouple's positions (right).

3.3. Freeze and thaw test:

The freeze and thaw (F&T) machine's time duration were one of the main concerns in the F&T test. In order to obtain the proper duration of the freezing and thawing cycles, the slab TC Control was designed and prepared with different thermocouple's location to monitor the temperature at different locations. According to the ASTM C-666, there are two methods for F&T testing; freezing and thawing in water (procedure A), or freezing in air and thawing in water (procedure B). First, the freezing and thawing in water were monitored. The results showed that the freezing duration for the center of the specimen, i.e. C7, to reach -18°C from the 4°C is about 19 hours and the thawing time is about 5 hours. The modified second procedure of ASTM C-666 was implemented for rapid F&T cycles; the concrete freezing procedure carries out without filling water and thawing procedure carries out with boiling water. Table 5 shows the real temperature changes of two cycles for one week, and Figure 27 shows the freeze and thaw cycle with procedure B during the three days.

Table 5 Temperature changes of two cycles for one week

Days	1 st cycle of a day		2 nd cycle of a day	
	MAX	MIN	MAX	MIN
Day 1	23.91	-15.62	24.34	-19.01
Day 2	36.5	-14.96	25.13	-16.45
Day 3	32.54	-15.46	18.57	-17.44
Day 4	31.46	-15.67	18.19	-17.3
Day 5	32.32	-15.6	24.32	-18.75
Day 6	16.57	-18.93	15.79	-19.15
Day 7	29.19	-16.75	20.71	-19.14
Day 8	13.52	-19.45	14.08	-19.3

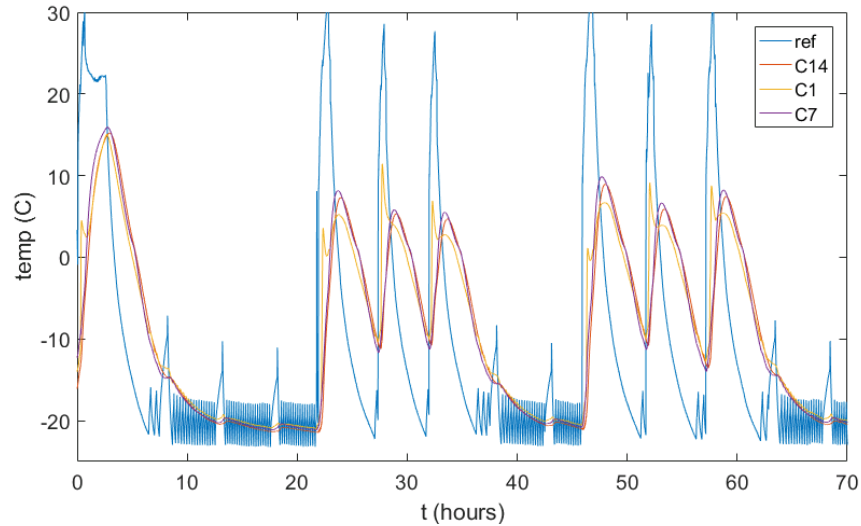


Figure 27. Freeze and thaw cycle with procedure B during the three days.

3.4. RACM sensor's sensitivity measurement

The RACM device development requires several parametric studies including the determination of the ultrasonic transmitter elevation, determination of the admissible signal averaging number, and the effectiveness assessment of the baffle with different materials.

Three configurations considered for the RACM system; RACM with absorbing baffle, RACM with diffusing baffle, and RACM with absorbing and diffusing baffle. For this purpose, wood was used as a diffusing material and sound barrier rubber foam was used to absorb the sonic waves. The result shows that the combination of absorbing and diffusing baffle provides more mechanical waves. Therefore, a baffle including diffusing and absorbing material used in the RACM testing. Figure 28 illustrates that using the baffles are beneficial. Therefore, two baffles, 1cm above the concrete specimens was used at both front and behind the transmitter was used to block the sound waves as much as possible.

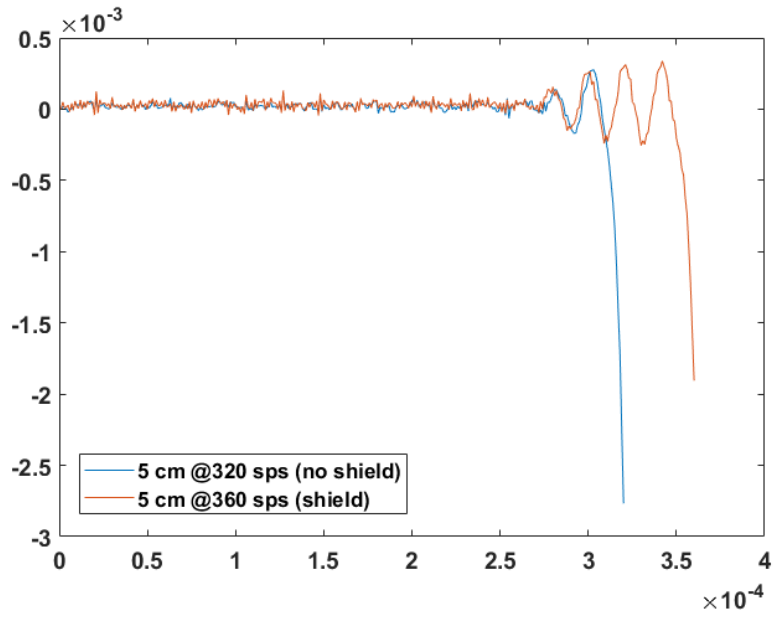


Figure 28. The advantage of using baffles to delay the sound wave arrival.

4. Test Procedures

4.1. Test Procedure's Overview

After the curing of the specimens, the specimen weight, actual size, first expansion measurement, first frequency test, MIRA, and RACM test were conducted and recorded as the initial testing results at the cycle 0. Then the specimens FT1, FT2, FT3, and PT were placed inside the freeze and thawing machine. Initially, the procedure A was used for freezing and thawing. However, since the trend of the degradation was significantly slow, the modified procedure B was carried out. The procedure B provides a harsher condition for specimens and also enables the PI to carry out 3 cycles per day. The modified procedure B freezes the concrete specimens in the air, and thaws the specimen by adding hot water. During this procedure, the concrete temperature was monitoring, using embedded thermocouples sensors. In this procedure, the concrete temperature was controlled to be $-10\text{ }^{\circ}\text{C}$ at freezing cycle and about $7\text{ }^{\circ}\text{C}$ at the thawing cycle. Once the specimen's temperature reaches $7\text{ }^{\circ}\text{C}$ the specimens were taken out of the F&T machine and the expansion test was conducted using the DEMEC strain gauge. Then the specimen's surfaces were dried and the resonant frequency test was conducted. Once the resonant frequency was carried out, the RACM test was conducted. Eventually, MIRA was the last test carried out on each testing.

Table 6. Test procedure

Steps	Procedure	Description
1	To place the concrete specimen in the F&T machine	The instrumentations are attached to the specimen.
2	To monitor the temperature during F&T cycle	The temperatures are measured by embedded thermocouples.
3	To take the specimen out of F&T machine and consider 30 minutes for drying	After ending each F&T cycle, specimens will be dried in the air within 30 minutes.
4	Test 1: Expansion test	Expansion test will be carried out for each direction.
5	Test 2: Resonant frequency test	This test will be done for slab and prism.
6	Test 3: RACM Test	Within 1 degree rotational intervals on the slab surface.
7	To place the concrete specimen in the F&T machine	For the next cycle
8	Data Analysis	Data analysis will be done on the results of all tests.

4.2. Expansion Measurement

A demountable mechanical strain gauge has advantages of accuracy, reliability, and cost over other methods of strain measurement. However, the desired accuracy is only obtained by the precision manufacture and care in the use of the instrument. With practice, 200 strains per hour

may be measured with an accuracy of about $\pm 5 \times 10^{-6}$ under most laboratory test conditions. Even greater accuracy has been obtained using the gauge in its ideal horizontal position and with the readings lying within a small range on the dial. In development tests of this kind 90 percent of measured strains were within $\pm 3 \times 10^{-6}$ of the mean. The instrument, which uses a lever and dial gauge arrangement mounted on an Invar Main Beam, is easy to use, and is located on 50 mm (EL35-2838) or 200 mm (EL35- 2846) gauge lengths which are formed by pairs of punched and drilled stainless steel discs (EL35-2854) glued to the surface under examination. The choice of material for the main beam and the reference bar has been determined by the requirement for a metal with a low coefficient of thermal expansion. Although many references in these notes are to concrete the instrument is suitable for use on a wide variety of materials and structure.

Any two rigid bodies, or two small, sensibly rigid, parts of an elastic body, may exhibit six degrees of freedom relative to each other, and an instrument which is designed to connect these two parts must, in general, allow these six movements in order to eliminate internal straining of the instrument. In the instrument under discussion two virtual point connections are used between the instrument and the specimen, and translational freedom between connections is provided by a moving arm pivoting about a knife edge and seating. The practical form of connection used is that of a cone locating into an initially cylindrical hole. Examination under a microscope shows that the first applications of the hardened cone, on the setting out the bar, into the hole cause plastic deformation of the steel seating and an approximately toroidal surface is produced. The combination of cone and toroid provides a fixed center of rotation about the x and y-axes as well as the z-axis for a sufficiently large range of angular movement to make the operation of the instrument satisfactory. The apex angle of the cone is 60 degrees. The 6.3 mm diameter stainless steel locating discs are blanked and the blind hole drilled 1 mm diameter. On any gauge length the rotation of the moving arm for various concrete strains is very small so that the cosine variation error of readings is negligible (0.3 percent for 1,000 lb/sq. in.) in concrete. A point of considerable interest in designing the instrument is to ensure that the locating force applied by the operator is directed along the axes of the instrument points. A subsidiary frame can be provided to ensure this but it has been found that so long as the handles of the instrument are placed so that no deformation is caused by the locating force, it is not difficult to eliminate, with practice, other sources of error such as horizontal thrust and variations of the instrument from the vertical. The dial used is a Mercer 254 Series.

One strain measuring per day is performed with proper accuracy under the most laboratory test conditions. The set up the gauge is a 30 mm length using reference bar and setting out the bar. Next, once the setting is done, the readings from four top sides of the specimens (Control, FT1, FT2 and FT3) are performed namely South, East, North and West and similarly from the four main sides by keeping the specimen on plain surface and connecting its edges with minimal pressure, required to provide good contact between the endpoints of the specimen. To make the operation of the instrument satisfactory, three readings are taken for one side and then averaging them for more accuracy, parallax error is avoided by ensuring that the gauge is held in a vertical plane. After

doing that, the average of two opposite sides of the top and the long sides are taken. shows expansion measurement of the slab specimens with a 3D view of the slab specimens with DEMEC bolts.

The specimens' length was measured using the following equation,

$$expansion (\%) = \left(\frac{L_i - L_o}{300 \text{ mm}} \right) \times 100, \quad (15)$$

where, the L_o is the expansion reading the cycle 0, L_i is the reading at the i th cycle.

4.3. Resonant frequency test

The resonant frequency test was carried out for the slab and the prism to measure the relative dynamic modulus of the concrete and to monitor the material degradation of the specimens. An impact was given to the center of the specimen and the transverse resonant frequency of the specimen was obtained through the accelerometer, placed at the 14.5 cm away from the impact point on the specimen according to the ASTM C215. The accelerometer was connected to the Kistler amplifier to increase the gain for 100 mV. Figure 29 shows the schematic of the resonant frequency test according to the ASTM C215, where the same configuration was also used for the slab specimens. The sampling rates used in this study is according to Table 7. Respect to the obtained fundamental frequency, the relative dynamic modulus of elasticity was calculated as follows,

$$P_C = (n_i^2 / n^2) \times 100, \quad (16)$$

where, P_C is the relative dynamic modulus of elasticity at cycle C, n_i is the fundamental transverse frequency at the cycle C, and n is the fundamental transverse frequency at cycle 0.

Table 7. Resonant frequency test parameters

Parameter	Sampling rate	Time duration	Dynamic range	Triggering level
Prism	200 kS/s	0.05 s (10000)	-10 to 10V (-20 V)	2V
Slab	200 kS/s	0.05 s (10000)	-10 to 10V (-20 V)	2V

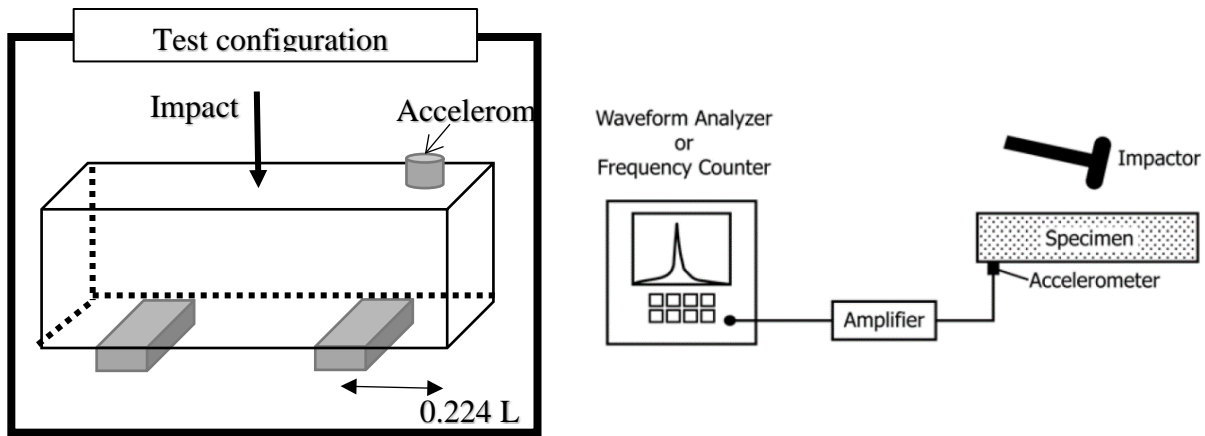


Figure 29. Resonant frequency test schematic

4.4. RACM Measurement

The RACM measurement was carried out within 40-degree intervals around the center of specimens at the distances 4, 6, and 8 cm. However, due to time limitation between the cycles, the 3 and 8 cm distances were measured at every 15 cycles. Two needles were installed on a transmitter and the backward MEMS sensor PCB to ensure the accuracy the pointing at each time. The device was oriented in a way that the transmitter needle aims the forward aim point, i.e. red point, and the backward needle aims the equivalent point on the other side of the circle, i.e. black point, depicted in Figure 30. The safe distance from the boundaries is considered as 10 cm where the reflection of the r-wave from the boundaries are not interfering the incident r-wave (elaborated in the specimen design section). The locations of the measurements are marked on the concrete specimen using a permanent marker. The measurements were carried out counterclockwise from the opposite side of the thermocouple location. Time averaging of 50 signals was imposed on the signal measurements. In addition, the signal averaging on the sensors arrays was conducted. The ultrasound integrated backscatter (IBS) calculation was carried out through the energy calculation of the measured signals with a developed MATLAB file discussed in the background & theory section. The testing parameters of the RACM is also provided in Table 8.

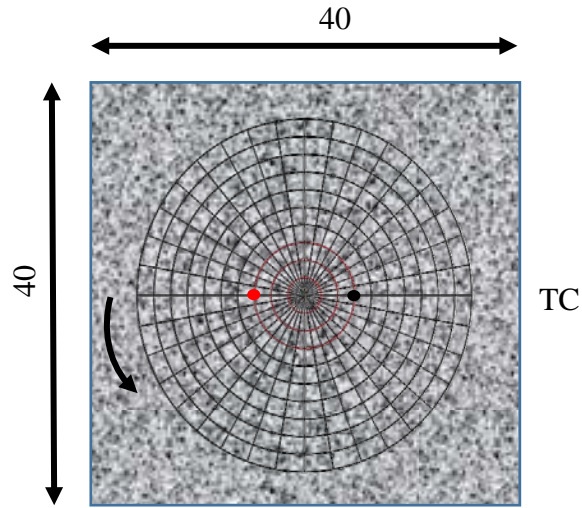


Figure 30. The RACM testing layout on the slab specimens

Table 8. RACM test parameters

Parameter	Sampling rate	Time duration (# of Sample)	Dynamic range	Triggering level
Control	1 MS/s	0.00038 (380)	10 mV	3
FT1	1 MS/s	0.00038 (380)	10 mV	3
FT2	1 MS/s	0.00038 (380)	10 mV	3
FT3	1 MS/s	0.00038 (380)	10 mV	3

4.5. MIRA Test

The MIRA test is performed to scan the concrete pavement and the propagated wave properties such as pavement thickness, stress wave speed, and intensity of wave propagation. Figure 31 shows the scanning direction and one of the field test pictures.

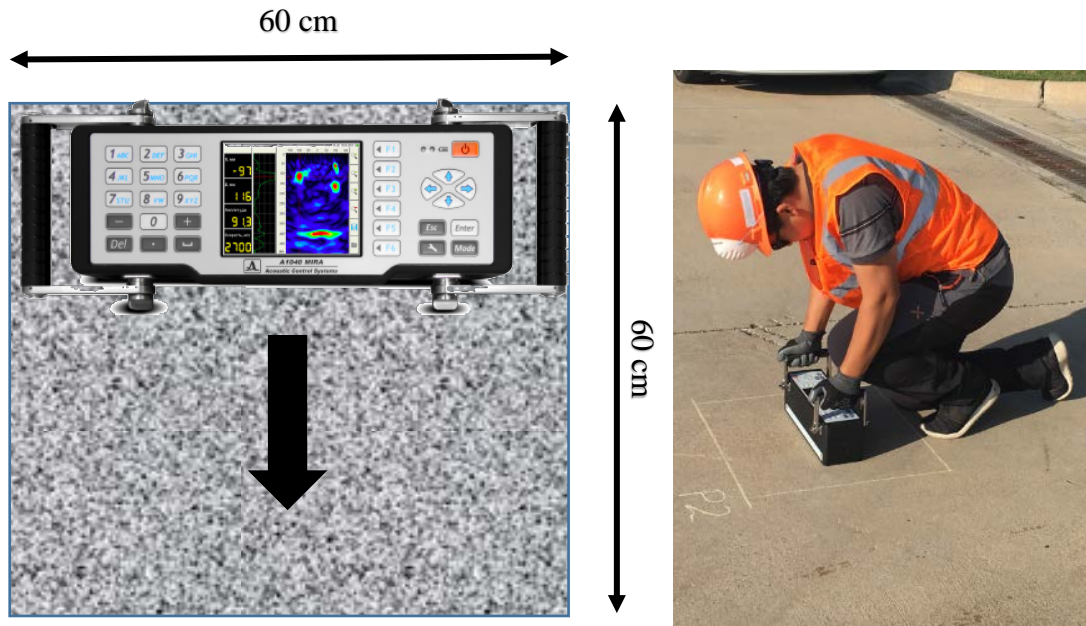


Figure 31. MIRA testing direction (left) and field test picture

5. System Analysis Software Development

The era of mobile technology opens the windows to the android app. The websites are vanishing, and the mobile phones are emerging. It's the time to change from conventional websites to apps, which has become the part of our daily routine. We are introducing "SMTL.apk" the android application software. The main aim of the mobile app is to allow fast access of our hardware remotely and to provide user-friendly environment to access, monitor, and control operational parameters. The android application is separated into two parts: the functional component (written in Java), and the graphical component (written in XML). The functional component forms the core of the app. It receives user input and performs all the calculations required. The graphical component, as the name implies, is simply the graphical user interface.

5.1. Methodology: Mobile Android APP

Mobility is at the core of every enterprise's digital strategy. There are numerous platforms offering easy mobile app development for Android, iOS, Windows and other operating systems. The Android OS, however, has progressed by leaps and bounds acquiring 87.7 percent of global market share. Android is free, and an open platform built on Linux. It is an open source solution for mobile devices offering a complete software stack including operating system, middleware, and key mobile applications. Apart from its speed, scalability, and performance, there are many other advantages of Android application development which includes:

- **Open Source:** The Android platform is open source which means the Android Software Development Kit (SDK) can be leveraged without having to worry about the licensing costs or royalty. Developers can interact with the Android developer community for the forthcoming versions which they can incorporate into their app development projects. These benefits make Android a lucrative prospect for enterprises, device manufacturers and wireless operators alike, resulting in rapid development of the applications.
- **Customizable User Interface:** A user interface can either make or break the app. Android-based applications are highly customizable and easier to manage. Google is highly focused on making its user interface customizable to help developers create custom Android apps for business. Being an open source platform, it allows developers to turn their creative ideas into reality and build innovative and interactive apps. It offers a wide array of customization options. Even the data management functions and multimedia tools can be easily updated to the app.
- **Low Investment & High ROI:** Android has a relatively low barrier to entry. Its Software Development Kit (SDK) is available for free to developers which significantly reduces the development costs. However, the app development costs can be bifurcated into three major parts: development, testing, and deployment. Developers are required to pay a one-time registration fee for application distribution. Thereafter, they can leverage any computer device to build and test the product on their smartphones, ensuring low investment and

increased engagement among users. Ultimately, users get an interactive app and the enterprise gains a higher return on investment.

- **Multiple Sales Channels:** Unlike other mobile platforms, Android applications can be deployed in different ways. Besides using Google Play Store and other third-party app marketplaces.
- **Easy to Adopt:** Android apps are scripted in Java programming language that leverages a rich set of libraries. Any developer familiar with Java can build Android applications easily. As per a developer survey, many Java experts find it easier to write apps for Android as compared to programmers with command over other programming languages.

Development of Android App and web-based platform needs several tools such as Python Anaconda, JRE, Eclipse (Helios), Android SDK, and Genymotion emulator. The details of tools are:

- **JRE:** Java runtime environment is a set of software tools for the development of Java applications. It combines the Java Virtual Machine (JVM), platform core classes and supporting libraries. JRE is part of the Java Development Kit (JDK).
- **JRE Eclipse (Helios):** Eclipse is an integrated development environment (IDE) used in computer programming and is the most widely used Java IDE. It contains a base workspace and an extensible plug-in system for customizing the environment.
- **Android SDK:** The Android SDK includes sample projects with source code, development tools, an emulator, and required libraries to build Android applications. Applications are written using the Java programming language and run on Dalvik, a custom virtual machine designed for embedded use which runs on top of a Linux kernel.
- **Genymotion emulator:** Genymotion is an easy-to-use Android emulator that has been designed to help app developers test their products within a safe, virtual environment
- **Python Anaconda-Spider:** Anaconda is a free and open source distribution of the Python and R programming languages for data science and machine learning related applications (large-scale data processing, predictive analytics, scientific computing), that aims to simplify package management and deployment.

In addition, Android, MySQL, and Python skills are required. The details of techniques are:

- **Android:** Application used to display our data in real time remotely from anywhere
- **MySQL:** Database used to store our data in proper table format and can be accessed anytime.

5.2. Methodology: a web-based platform

With web-based applications, users access the system via a uniform environment—the web browser. While the user interaction with the application needs to be thoroughly tested on different web browsers, the application itself needs only be developed for a single operating system. There is no need to develop and test it on all possible operating system versions and configurations. This makes development and troubleshooting much easier and for web applications that use

a flash front-end testing and troubleshooting are even easier. Unlike traditional applications, web systems are accessible anytime, anywhere and via any PC with an Internet connection. This puts the user firmly in charge of where and when they access the application. It also opens up exciting, modern possibilities such as global teams, home working, and real-time collaboration. The idea of sitting in front of a single computer and working in a fixed location is a thing of the past with web-based applications. The user interface of web-based applications is easier to customize than is the case with desktop applications. This makes it easier to update the look and feel of the application or to customize the presentation of information to different user groups. Therefore, there is no longer any need for everyone to settle for using exactly the same interface at all times. Instead, it can be found the perfect look for each situation and user. With the web-based approach installation and maintenance becomes less complicated too. Once a new version or upgrade is installed on the host server all users can access it straight away and there is no need to upgrade the PC of each and every potential user. Rolling out new software can be accomplished more easily, requiring only that users have up-to-date browsers and plugins. As the upgrades are only performed by an experienced professional to a single server the results are also more predictable and reliable. Web-based applications are typically deployed on dedicated servers, which are monitored and maintained by experienced server administrators. This is far more effective than monitoring hundreds or even thousands of client computers as is the case with desktop applications. This means that security is tighter and any potential breaches should be noticed far more quickly. Any of three core technologies can be used for building web-based applications, depending on the requirements of the application. The newer Microsoft .NET platform uses Active Server Pages, SQL Server, and .NET scripting languages. The third option is the Open Source platform, which is best suited to smaller websites and lower budget applications. The web-based platform design needs a web server and Python programming skills. The web server was used Amazon Web Services (AWS); Amazon Web Services is a comprehensive, evolving cloud computing platform provided by Amazon. It provides a mix of infrastructure as a service (IaaS), platform as a service (PaaS) and packaged software as a service (SaaS) offerings.

5.3. Design and process

Figure 32 shows a case diagram for an Android app which pops up with a Google Maps when the user opens the app and it also allows to select the location from the app whose data a user wants to see. Once it is done, the next page will show the type of specimen to be observed which will be shown in the form of lists.

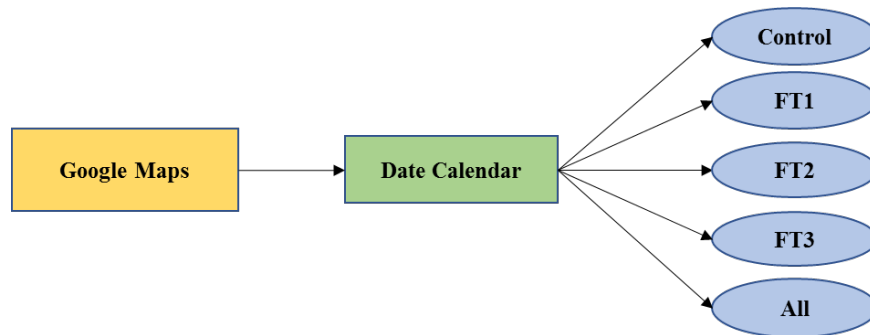


Figure 32 Case diagram for the main screen

As shown in Figure 33, once the specimen has been selected by the user, the next page will show the type of tests that have been conducted on that specimen. For example RACM, resonant frequency or expansion test. The final result graph or data sheet is plotted at the last window when one of the test results are selected.

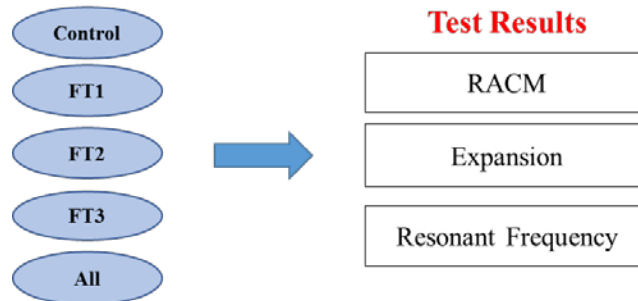


Figure 33 Case diagram for the menu screen

The App opens with Google maps, which is integrated with Google API using Google key. The XML file is used to specify the orientation of the layout using different layouts. Figure 34 shows the relative layout for Android Google maps. The fragment section indicates the namespace, width, and height of the map on Android screen.

```
<RelativeLayout android:layout_height="match_parent"
    android:layout_width="match_parent"
    xmlns:android="http://schemas.android.com/apk/res/android">

    <fragment xmlns:android="http://schemas.android.com/apk/res/android"
        xmlns:map="http://schemas.android.com/apk/res-auto"
        xmlns:tools="http://schemas.android.com/tools"
        android:id="@+id/map"
        android:name="com.google.android.gms.maps.SupportMapFragment"
        android:layout_width="match_parent"
        android:layout_height="match_parent"
        tools:context="com.example.kapil.my_first_app.MainActivity" />

</RelativeLayout>
```

Figure 34. screen shot of the XML code : Relative layout for Android Google maps

Table 9 shows the steps to acquire the Android Google maps key, and Figure 34 show the script of API key.

Table 9. The steps to acquire the Android Google maps key

Steps	
1	Go to the Google Cloud Platform Console.
2	Create or select a project.
3	Click Continue to enable the Maps SDK for Android.
4	On the Credentials page, get an API key.
5	From the dialog displaying the API key, select Restrict key to set an Android restriction on the API key.

6	In the Restrictions section, select Android Apps, and then enter the App's SHA-1 fingerprint and package name.
7	Click Save.
8	Add the API key to the Application in AndroidManifest.

```
android:name="com.google.android.geo.API_KEY"
android:value="AIzaSyB6eRLreY2K0j1M5U7YzRsNOP10spnG9g" />
```

Figure 35. API key

For this XML, the Java code is written as a back-end for functionality as shown in Figure 36. The different testing location, which has the result data required to be displayed are defined using the marker in Java. The function used to define markers is ‘OnMapReady’, which is a call back function, and it is called when map got open. In this function, an instance of the map is taken into the variable mMap. Then, the style is set using ‘map style’ for a better user interface. Next line is to add the marker by defining its position, title and tag. To add a marker, the function used in Java is ‘add Marker’ and it needs three parameters as input and the position coordinates are obtained from Google maps. The location information in the code is shown below:

```
private static final LatLng Nedderman_hall = new LatLng(32.732722, -97.113856);
private static final LatLng MAC = new LatLng(32.732090, -97.117461);
private static final LatLng CELB = new LatLng(32.727875, -97.125529);
private static final LatLng CPC = new LatLng(32.730537, -97.108105);
private static final LatLng UTA = new LatLng(32.730230, -97.113427);
```

```
@Override
public void onMapReady(GoogleMap googleMap) {
    mMap = googleMap;
    // Add a marker in Sydney and move the camera
    mMap.setMapStyle(MapStyleOptions.loadRawResourceStyle(context, R.raw.mapstyle));

    myMarker = mMap.addMarker(new MarkerOptions().
        position(Nedderman_hall)
        .title("Nedderman Hall"));
    myMarker.setTag(0);

    myMarker = mMap.addMarker(new MarkerOptions().
        position(MAC)
        .title("Maverick Activity Stadium"));
    myMarker.setTag(0);

    myMarker = mMap.addMarker(new MarkerOptions().
        position(CELB)
        .title("UTA CELB"));
    myMarker.setTag(0);

    myMarker = mMap.addMarker(new MarkerOptions().
        position(CPC)
        .title("College park centre"));
    myMarker.setTag(0);

    myMarker = mMap.addMarker(new MarkerOptions().
        position(UTA)
        .title("University of Texas at Arlington"));
    myMarker.setTag(0);
}
```

Figure 36. Back-end Java code

The added five of markers on the map is shown in Figure 37.

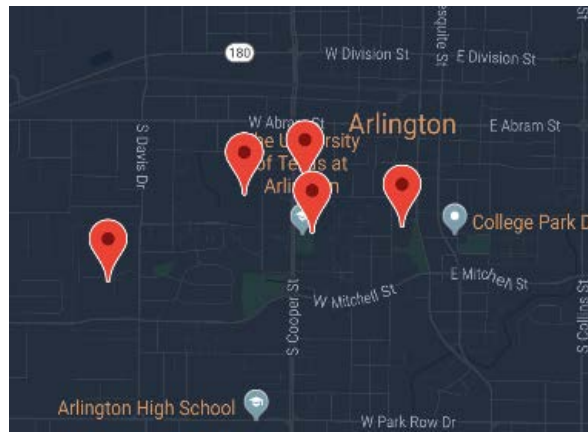


Figure 37. Google map with the marked five different locations

Next step is to add the marker listener, which is used to show what will happen when any location is clicked in the map. Once the user clicks on any location, it will pop-up a calendar window, which allows the user to select the date. The Calendar window is added using 'setOnMarkerClickListener' as shown in below Figure 38 (left). Since the test results are updated different day, the calendar function is required for the system. Date selection and new activity are started as per the code is written in 'mDateSetListener'. The function checks whether the user has selected all three parameters in YY/MM/DD format as shown in Figure 38 (right).

```
mMap.setOnMarkerClickListener((marker) -> {
    System.out.println(marker.getTitle());
    Calendar cal = Calendar.getInstance();
    int year = cal.get(Calendar.YEAR);
    int month = cal.get(Calendar.MONTH);
    int day = cal.get(Calendar.DAY_OF_MONTH);

    DatePickerDialog dialog = new DatePickerDialog( context: MapsActivity.this,
        android.R.style.Theme_Holo_Light_Dialog_MinWidth,
        mDateSetListener,
        year, month, day);
    dialog.getWindow().setBackgroundDrawable(new ColorDrawable(Color.TRANSPARENT));
    dialog.show();
    return true;
});

mDateSetListener = (OnDateSetListener) (view, year, month, day) -> {
    Intent intent=new Intent( packageContext: MapsActivity.this,Blocks.class);
    startActivity(intent);
    overridePendingTransition(R.anim.right_in, R.anim.left_out);
};
```

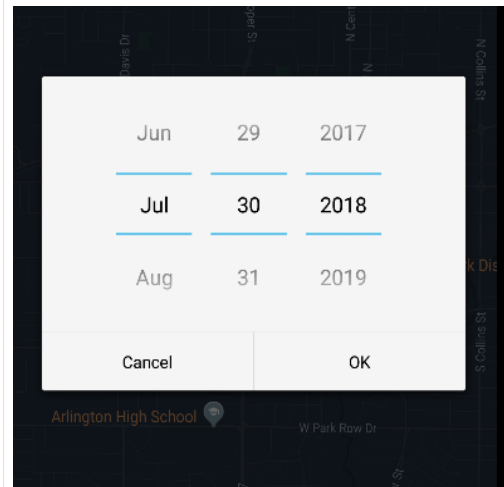


Figure 38. Calendar window: code using 'setOnMarkerClickListener' (left) and screen shot of date selection window (right)

The next step is 'Blocks.Java', which is used to represents the orientation of different specimens. As shown in Figure 39, the five text views: Control, FT1, FT2, FT3 and All were applied to the specimen selection window. In the text view, the width, height, gravity, text name for each specimen was given as the details. The Java code for this XML is written using View.

OnClick listener, which is a call back function that is triggered when any specimen is clicked. The specimens are identified by their id in the XML file so for e.g. on clicking FT2 it will look for its id defined in XML in our case it is R.id.ft2 and corresponding activity will be intended. The action after clicking the specimen case button is defined in this function, and a new window will show up the test conducted on that specimen in the form of the lists. The specimen corresponding count is assigned to that specimen which will be used further to plot the graph.



Figure 39. Specimen selection window

Next Once the user selects the specimen, a new activity will start to show the type of test conducted on that specimen. This page indicates the type of test conducted which are IBS (RACM), resonant frequency test and expansion as shown in the bottom of Figure 40, and the top figure of Figure 40 is the code for the test result plotting.


```
String[] NAMES = {"IBS", "Resonant Test", "Expansion"};
ListAdapter kapilAdapter = new ArrayAdapter<String>(context this, android.R.layout.simple_list_item_1, NAMES);
ListView KapilsListView = (ListView) findViewById(R.id.SpcimensListView);
KapilsListView.setAdapter(kapilAdapter);

//now we will create onclick listener
KapilsListView.setOnItemClickListener((adapterView, view, position, l) -> {

    if (position == 0) {
        Intent myIntent = new Intent(view.getContext(), Freq_graph.class);
        startActivityForResult(myIntent, requestCode: 0);
        overridePendingTransition(R.anim.right_in, R.anim.left_out);
    }
    if (position == 1) {
        Intent myIntent = new Intent(view.getContext(), Bar_graph.class);
        startActivityForResult(myIntent, requestCode: 0);
        overridePendingTransition(R.anim.right_in, R.anim.left_out);
    }
    if (position == 2) {
        Intent myIntent = new Intent(view.getContext(), Point_chart.class);
        startActivityForResult(myIntent, requestCode: 0);
        overridePendingTransition(R.anim.right_in, R.anim.left_out);
    }
});
```

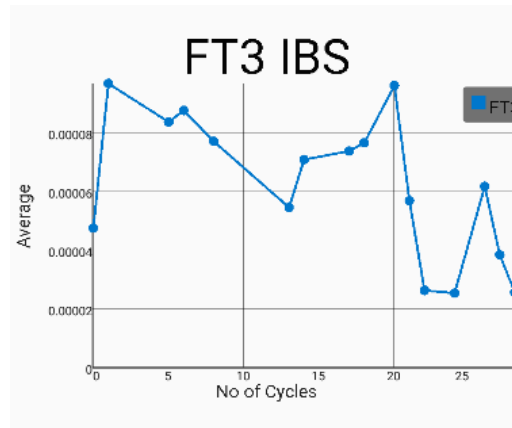


Figure 40. Example of test result code (top) and IBS (RACM) test result window (bottom)

The task is to plot the graph in the Android App. The graph view library is used to plot the graph in Android Apps to plot the graphs. Figure 41 XML code shows the linear layout function.

```

<?xml version="1.0" encoding="utf-8"?>
<LinearLayout xmlns:android="http://schemas.android.com/apk/res/android"
    xmlns:tools="http://schemas.android.com/tools"
    android:id="@+id/activity_freq_graph"
    android:layout_width="match_parent"
    android:layout_height="match_parent"
    android:orientation="vertical"
    android:gravity="center"
    tools:context="com.example.kapil.my_first_app.Freq_graph">

    <com.jjoe64.graphview.GraphView
        android:layout_width="400dp"
        android:layout_height="300dip"
        android:layout_marginTop="24dp"
        android:id="@+id/graph"
        android:layout_alignParentBottom="true"
        android:layout_alignParentTop="true"/>

</LinearLayout>

```

Figure 41. Linear layout function

The Java code to plot the graph is as shown in Figure 42. The CVS format file related to the block number and result is stored in the assets folder of our App. All the data is stored in the CSV file, and it keeps updating on daily basis using python code. This data is used to plot the graph into an Android App remotely. Based on the selected file, the title of the graph is set and plotted with the graph.

```

mGraph = (GraphView) findViewById(R.id.graph);
mGraph.removeAllSeries();

if(Blocks.count <= 3) {
    try {
        if (Blocks.count == 0) {
            inputStream = getAssets().open( fileName: "Control_IBS.csv");
            mGraph.setTitle("Control IBS");
        } else if (Blocks.count == 1) {
            inputStream = getAssets().open( fileName: "FT1_IBS.csv");
            mGraph.setTitle("FT1 IBS");
        } else if (Blocks.count == 2) {
            inputStream = getAssets().open( fileName: "FT2_IBS.csv");
            mGraph.setTitle("FT2 IBS");
        } else if (Blocks.count == 3) {
            inputStream = getAssets().open( fileName: "FT3_IBS.csv");
            mGraph.setTitle("FT3 IBS");
        } else {

        }

        BufferedReader br = new BufferedReader(new InputStreamReader(inputStream));

```

Figure 42. Plotting graph Java code

The while loop and declaration script are shown in Figure 43. The X and Y values are set by the stored data array. To plot on the graph, the feature called 'Datapoint' which will run the for loop depending on the size of an array is used, and the axis data is plotted on the graph as shown in Figure 44, which is the expansion test result graph.

```

ArrayList<DataPoint> arrDataPoint = new ArrayList<>();
while ((line = br.readLine()) != null) {
    content = line.split( regex: ",", );
    if (LineNumber == 0) {
        minValues[0] = Double.parseDouble(content[0]);
    }
    LineNumber++;
    calculateMinAndMax(content);
    Xval = Double.parseDouble(content[1]);
    Yval = Double.parseDouble(content[11]);
    DataPoint dp = new DataPoint(Xval, Yval);
    arrDataPoint.add(dp);
    //csvLine.add(content);
}
DataPoint[] listDp = new DataPoint[arrDataPoint.size()];
for (int i = 0; i < arrDataPoint.size(); i++) {
    listDp[i] = arrDataPoint.get(i);
}
LineGraphSeries<DataPoint> series = new LineGraphSeries<>(listDp); }

private void calculateMinAndMax(String[] line) {
    for (int i = 0; i < line.length; i++) {
        //check the max value
        double currentValue = Double.parseDouble(line[i]);
        //System.out.println(line.length);
        if(currentValue > maxValues[i] ) {
            maxValues[i] = currentValue;
        }
        //minValues[i] = currentValue;
        //check the min value
        if(currentValue < minValues[i]) {
            minValues[i] = currentValue;
        }
    }
}

```

Figure 43. While loop (left) and declaration (right) of Java script to create arrays

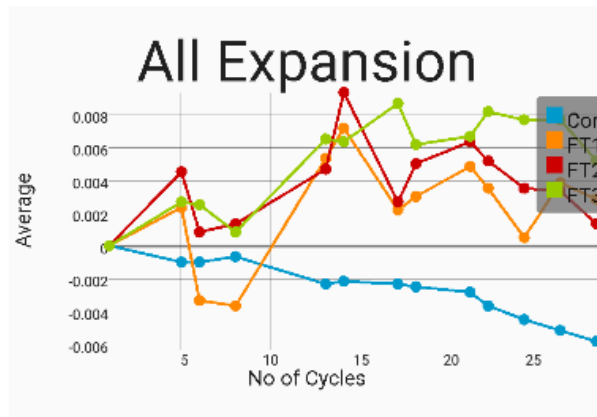


Figure 44. Example of expansion test result

The procedure to realize the Android application is introduced on Appendix B.

6. Results and Discussion

6.1. Laboratory Tests

6.1.1. Expansion test

The expansion test is conducted according to the test procedure, 4.2 Expansion Measurement. The control specimen, which is cured at the 77 °F temperature controlled and dried condition, shows 0.01 shrunk strain value in the period as shown in Figure 45. The tendency indicates the concrete shrink phenomenon in the typical curing condition.

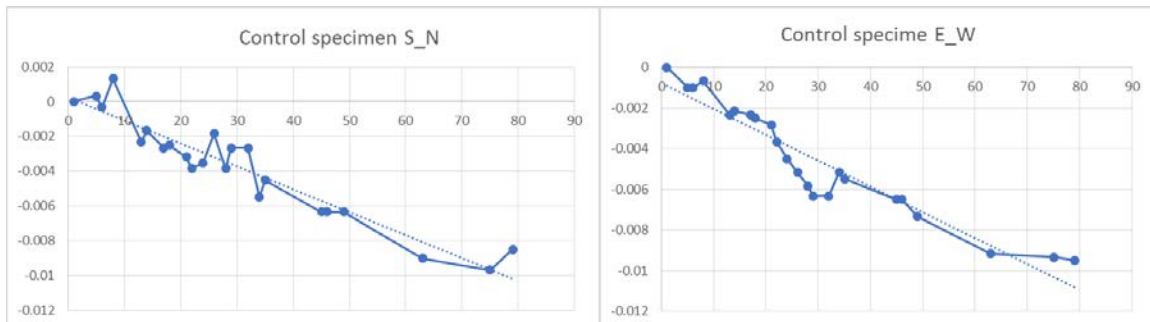


Figure 45. Expansion test result of the control slab specimen

On the contrary, the controlled specimens, FT2, and FT3 show the increased trend line as shown in Figure 46. However, the tendencies are relatively weaker than the control specimen expansion test result.

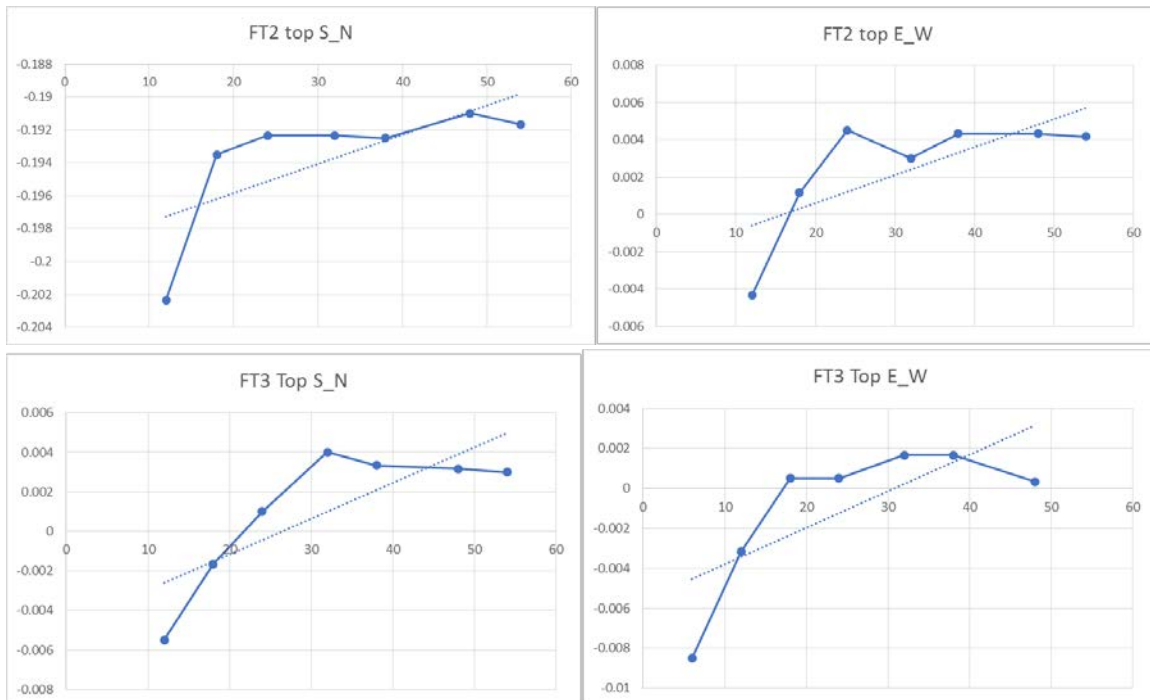


Figure 46. Expansion test result of the control specimen: FT2 (top) and FT3 (bottom)

6.1.2. Resonant frequency test

The test result of resonant frequency test of prism specimen is shown in Figure 48. The prism specimen was cycled with other concrete specimens. The damage on the prism specimen is extremely larger than FT concrete block after 200 cycles as shown in Figure 47.



Figure 47. Surface of cycled prism concrete specimen, PT1

The resonant frequency of the prism specimen is continuously decreased after casting concrete 1800 Hz to 1260 Hz while 140 F&T cycles, and it is about 30% decreased resonant frequency value as shown in Figure 48.

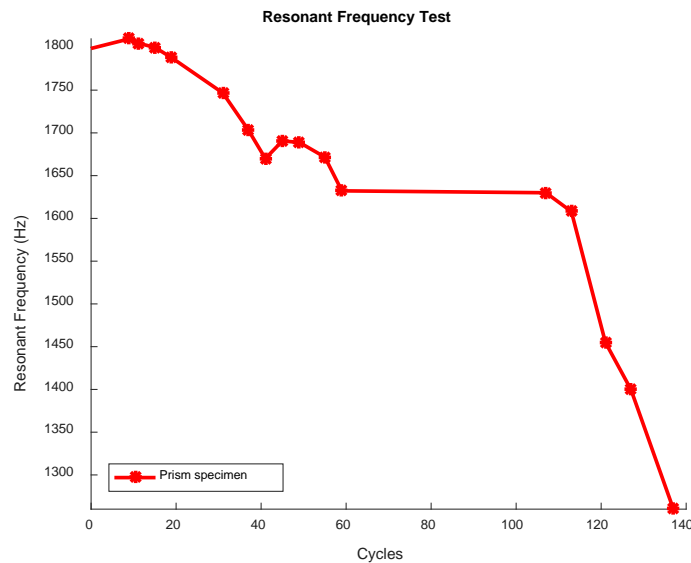


Figure 48. Resonant frequency test result of prism specimen

The test result of a resonant frequency test is shown in Figure 49. The resonant frequency of control specimen shows 2975 - 3000 Hz range and doesn't show any tendency. The difference between the maximum and minimum resonant frequency value is 25 Hz, and it is 0.8% decreased value. The resonant frequency of F&T cycled FT2 is decreased. The difference between the

maximum and minimum resonant frequency value is 255.3 Hz, and it is 8.7% decreased value. The resonant frequency of F&T cycled FT3 shows a similar tendency to the FT2 specimen. The resonant frequency of those cycled specimens is decreased. The difference between a maximum and minimum resonant frequency value is 286.7 Hz, and it is 10% decreased value. The control specimen and cycled specimen show different starting frequency. Thus, the early age concrete is significantly affected by the F&T damage.

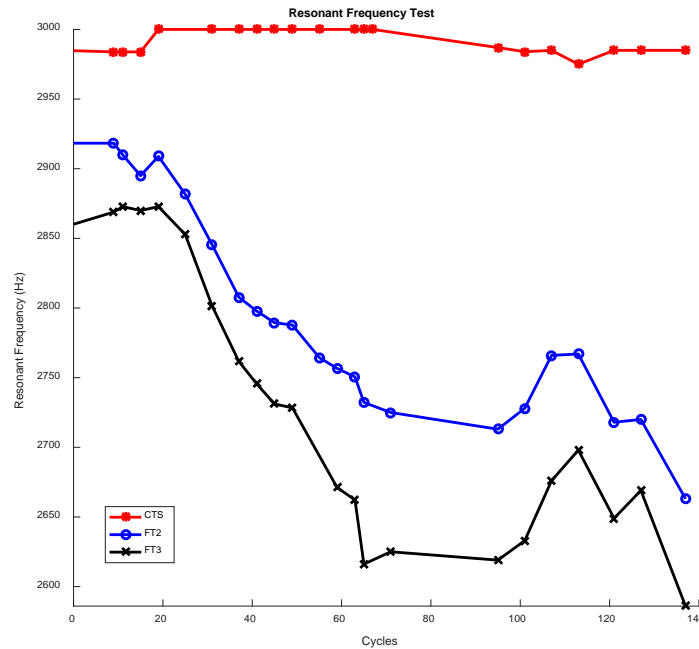


Figure 49. Resonant frequency test result of concrete specimens

6.1.3. RACM (IBS) test

The signal analysis was performed in accordance with 1.1 theory of backscattered wave detection. The backscattered mechanical waveforms of CTS, which is the control specimen, FT2, and FT3, which are cycled specimens, and PMMA, which is poly (methyl methacrylate) material were obtained by the RACM test. The PMMA mechanical waves show bigger amplitude than the concrete specimen. The three concrete specimens show similar amplitude and waveform. The B_e value was obtained by the waves of the backward propagated wave.

The backscattered waves can be obtained by subtracting the average of mechanical waves, which is propagated to backward. Since every ultrasound emission energy is not exactly the same, the average subtracted signal will be divided by forwarding propagated wave energy as mentioned in the theory. The average subtracted signal, which is considered forward propagated waver energy, is shown in Figure 52, and it is backscattered waves. The amplitude of PMMA backscattered waves shows smaller than concrete specimens. The cycled concrete specimens, FT2 and FT3, show

higher values of backscattered waves. The energy values of backscattered waves are 0.103 of control specimen, 0.162 of FT2, 0.154 of FT3, and 0.049 of PMMA.

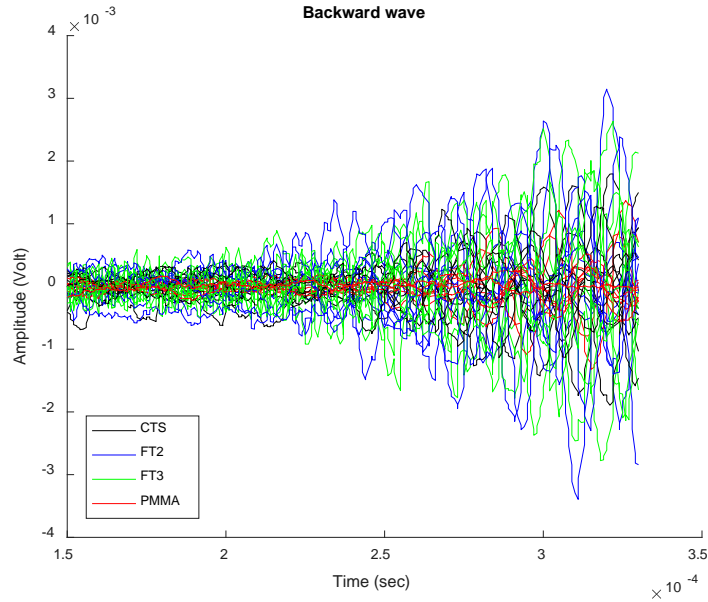


Figure 50. Backscattered of CTS, FT2, FT3, and PMMA specimen

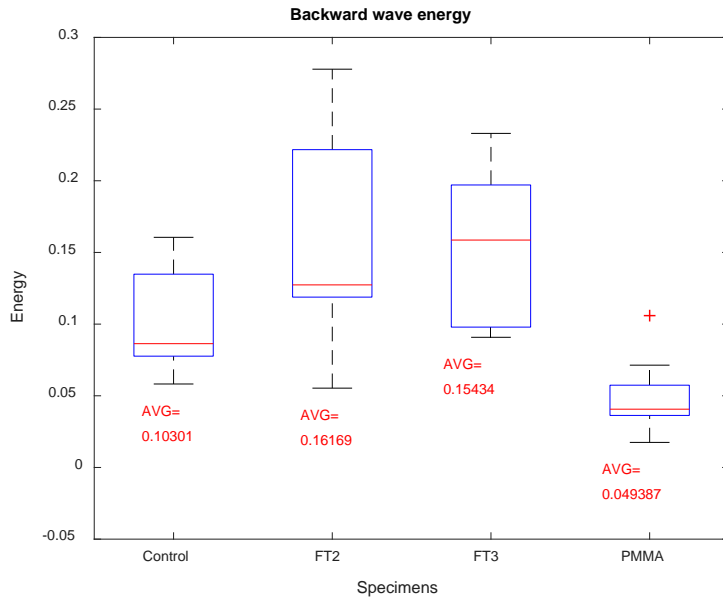


Figure 51. Energy boxplot of specimens

The backscattered energy tendency and resonant frequency test results of laboratory test specimens while 95 to 135 cycles are shown in Figure 52. CTS, FT2, and FT3 test results are compared on the graph. The backscattered energy and resonant frequency changes show a different tendency. In the case of the backscattered wave energy, both cycled specimens show the increased

tendency, which indicates the scattered wave energy to the backward by the cracks inside of concrete specimen are gradually increased. On the contrary, resonant frequencies are gradually decreased by the concrete inner damage. In both cases, the controlled concrete specimen shows insensitivity changes. The solid lines are the backscattered wave energy and marked dotted lines are resonant frequency test results.

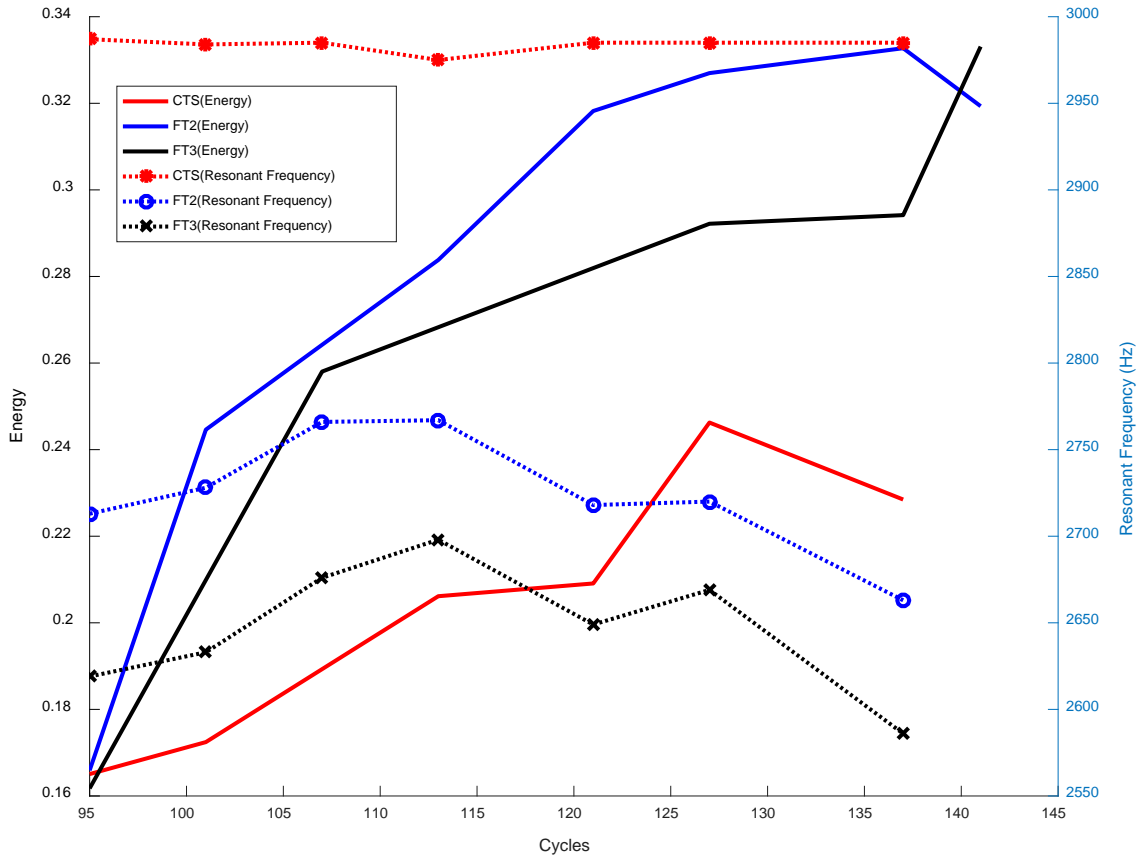


Figure 52. Backscattered energy and resonant frequency tendency of laboratory test specimens

6.2. Field Tests

For the field test, PI work with roadways for pavement and bridge tests in the local Texas area. The results were compared and evaluated with tests results obtained from the other advanced NDE methods. Damage monitoring will be demonstrated over a period of two months. The field tests were performed for the different types of concrete pavement. The target was parking lots, bridge road, and pedestrian. RACM and MIRA tests were conducted.

6.2.1. Pedestrian

The pedestrian concrete pavement was chosen near the UTA campus on S. Davis Dr. (32.730568, -97.123660), and the site and location are shown in Figure 53. The tests on the recently constructed pedestrian and existing pedestrian concrete pavements were performed at the same location. The test was conducted at 3 days after the construction in case of the relatively new pedestrian. The condition of pedestrians is shown in Figure 54.



Figure 53. Site of pedestrian: satellite map (left) and site photo (right)



Figure 54. Pedestrian condition: old pedestrian (left) and recently constructed pedestrian (right)

Figure 55 shows the RACM and MIRA testing on the pedestrian concrete pavements.

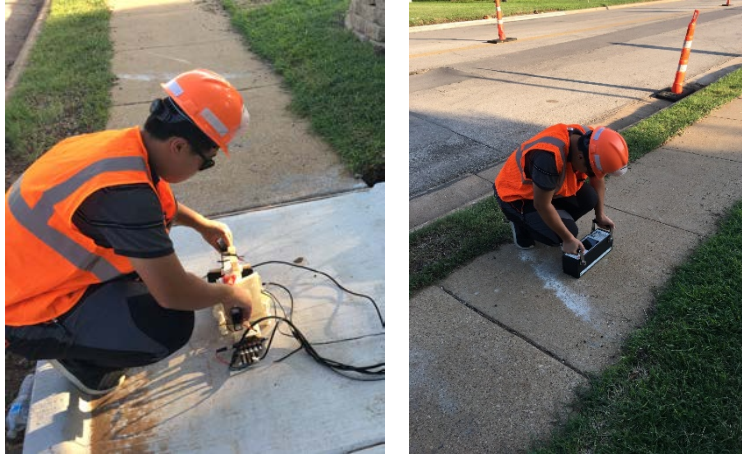


Figure 55. RACM (left) and MIRA (right) test on the pedestrian concrete pavement

MIRA result image is shown in Figure 56. Thicknesses of existing and recently constructed pedestrians were measured about 105 mm and 130 mm respectively, and the shear wave speeds were measured 2530 m/s and 2490 on the pedestrian concrete pavements.

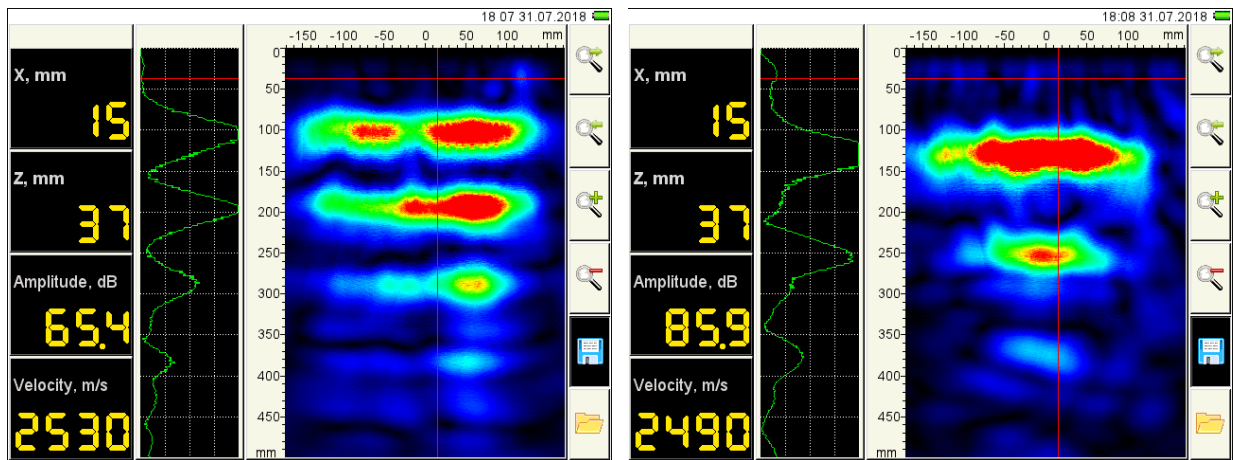
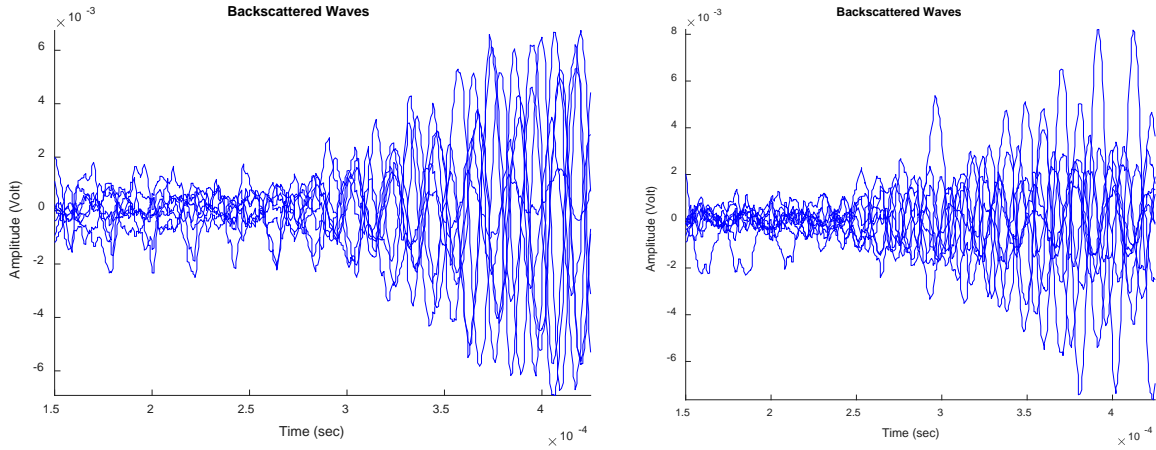


Figure 56. MIRA result image on the pedestrian: existing pedestrian (left) and recently constructed pedestrian (right)

The 0.8273 and 0.6149 backscattered energies of existing and recently constructed pedestrians were obtained, and the backscattered waves are shown in Figure 57.



Backward wave energy

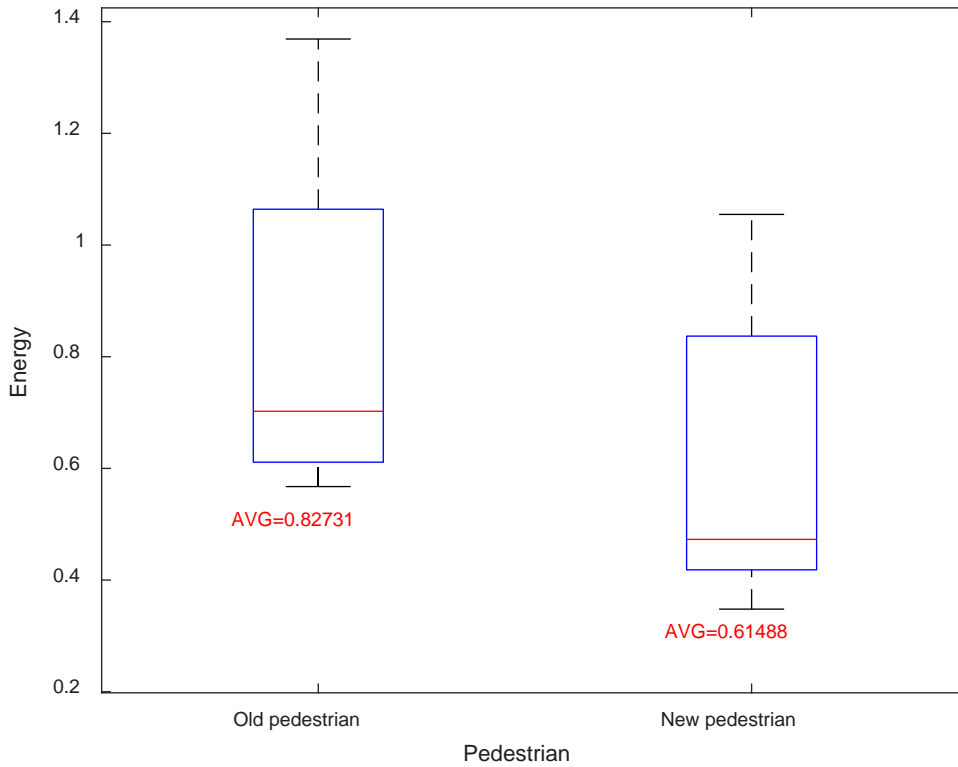


Figure 57. Backscattered waves of pedestrian sites: existing pedestrian (top left), recently constructed pedestrian (top right), and boxplots of backscattered wave energy (bottom)

6.2.2. Parking lots

The parking lots located in 1221 W Mitchell St, Arlington, TX 76013, UTA civil engineering laboratory building (32.727740, -97.125928) was chosen, and the site map is shown in Figure 58.



Figure 58. Site of parking lots: satellite map (left) and site photo (right)

Figure 59 shows the RACM and MIRA testing on the parking lot site.



Figure 59. RACM (left) and MIRA (right) test on the parking lot site

MIRA result image is shown in Figure 60. Thickness was measured about 180 mm, and the shear wave speed is measured 2530 m/s on the parking lots concrete pavement.

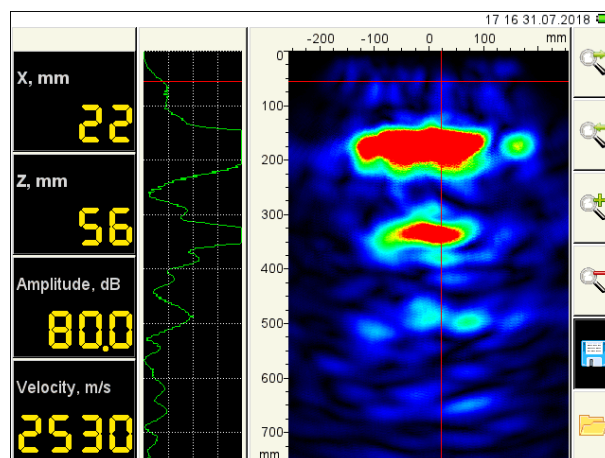


Figure 60. MIRA result image on the parking lot site

The 0.4838 backscattered energy was obtained on the parking lot site, and the backscattered waves are shown in Figure 61.

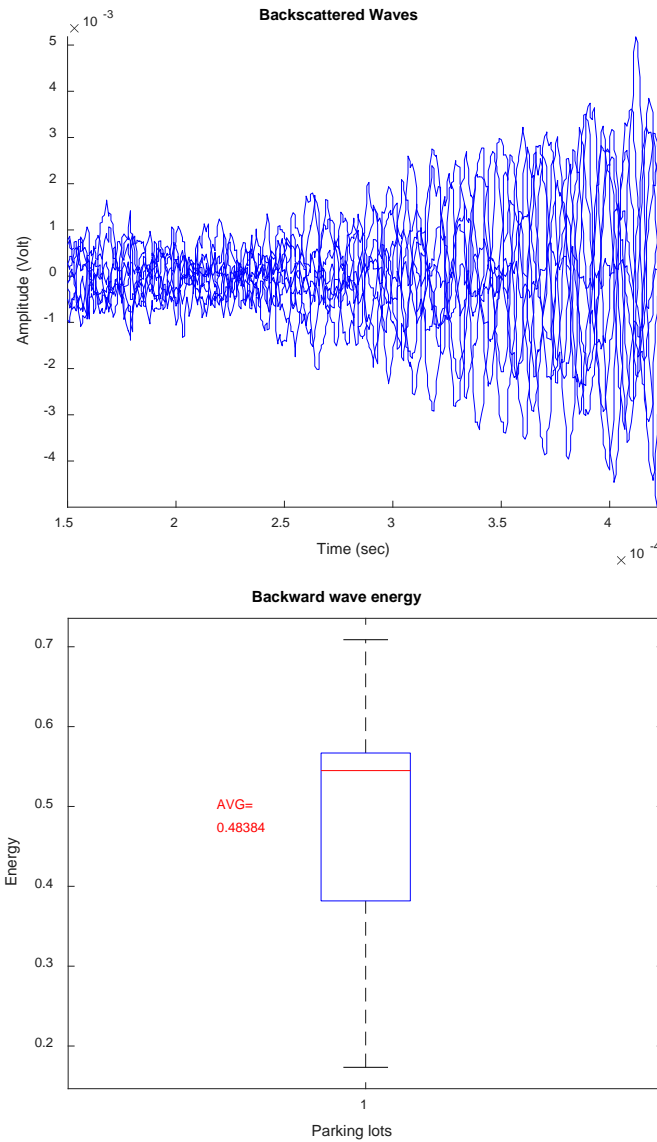


Figure 61. Backscattered waves and energy boxplot of parking lot site

6.2.3. Bridge road

The bridge road concrete pavement is in the intersection of South Coopers Street and West Mitchell Street (32.727565, -97.114509) was chosen near the UTA campus, and the site and location are shown in Figure 62.



Figure 62. Site of bridge road: satellite map (left) and site photo (right)

Figure 63 shows the RACM and MIRA testing on the bridge road.

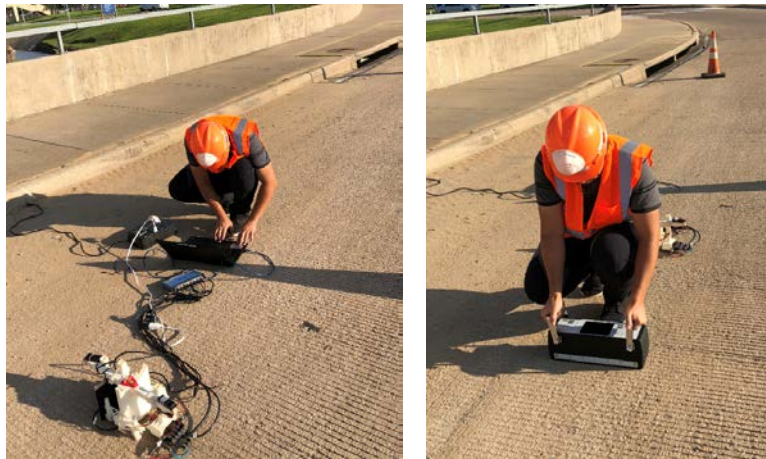


Figure 63. RACM (left) and MIRA (right) test on the bridge deck

MIRA result image is shown in Figure 64. Thickness was measured about 210 mm, and the shear wave speed is measured 2650 m/s on the bridge road concrete pavement.

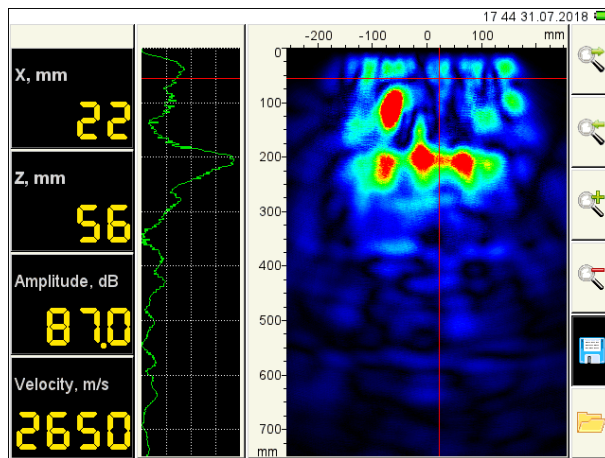


Figure 64. MIRA result image on the parking lot site of bridge site

The 2.4593 backscattered energy was obtained on the bridge road site, and the backscattered waves are shown in the top wave graphs of Figure 65, and the backscattered wave energies are shown in the bottom boxplot.

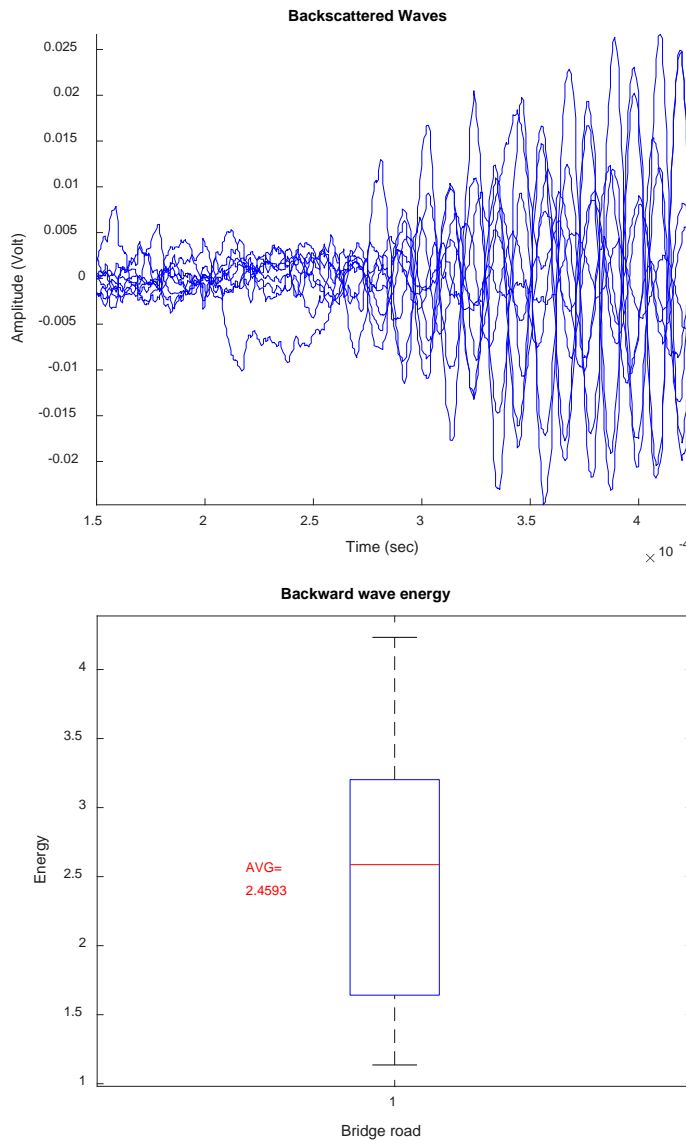


Figure 65. Backscattered waves and energy boxplot of bridge site

6.3. Web-based Platform

The results of the project are uploaded on the web-based platform: <http://ec2-54-218-48-75.us-west-2.compute.amazonaws.com/>. Total 8 pin points are marked to show the laboratory test result and field test as shown in Figure 66.

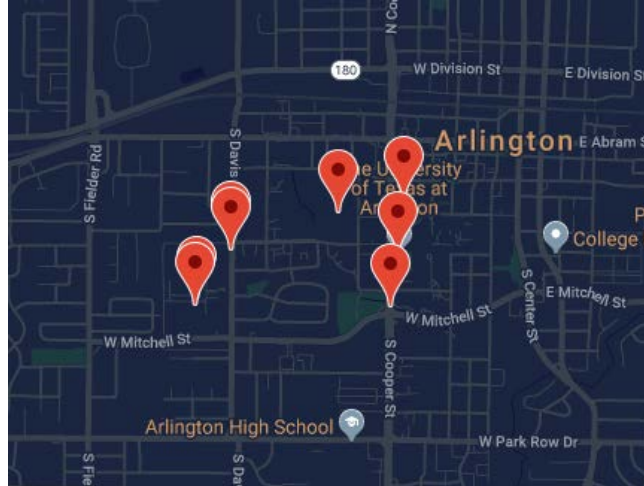
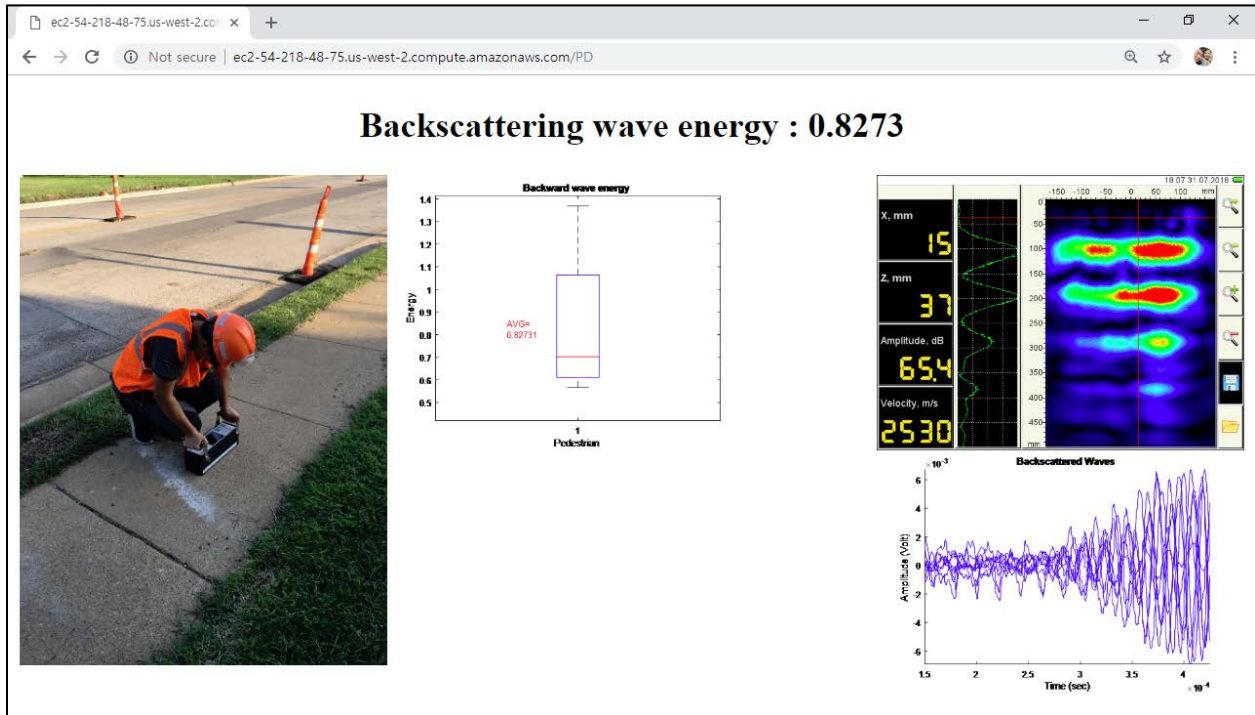
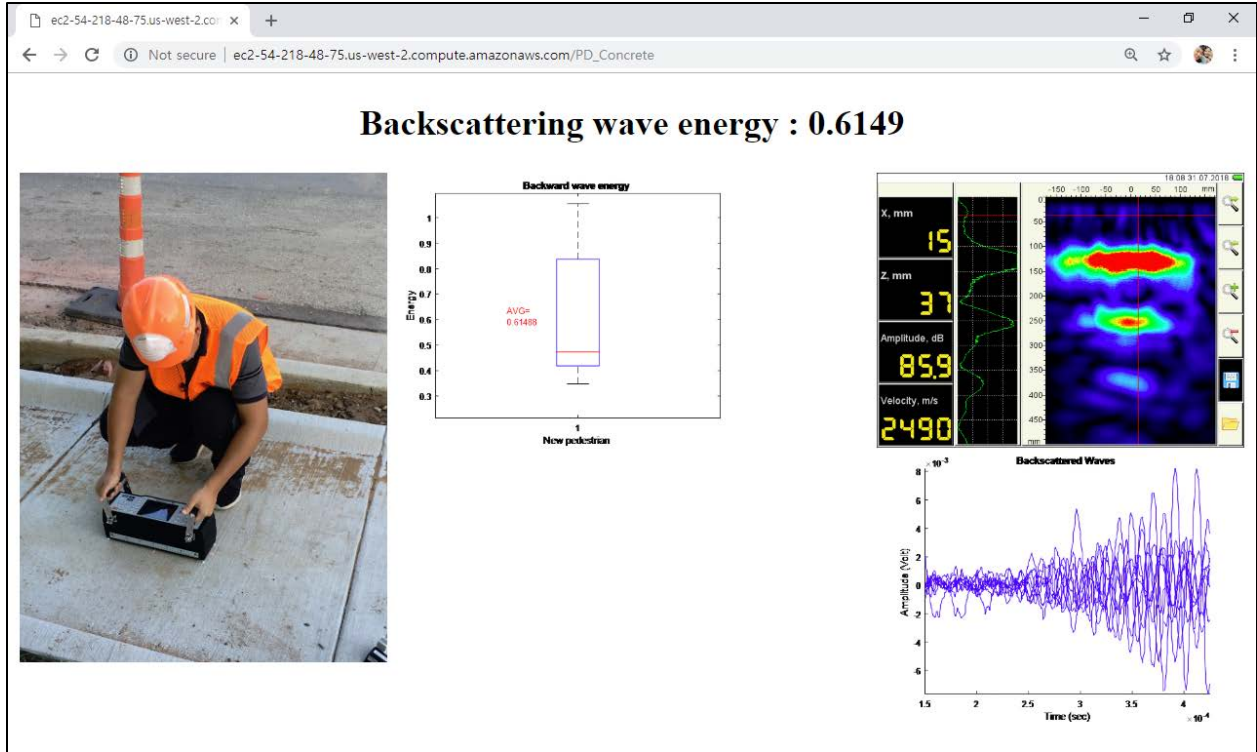


Figure 66. Main page of the web-based platform

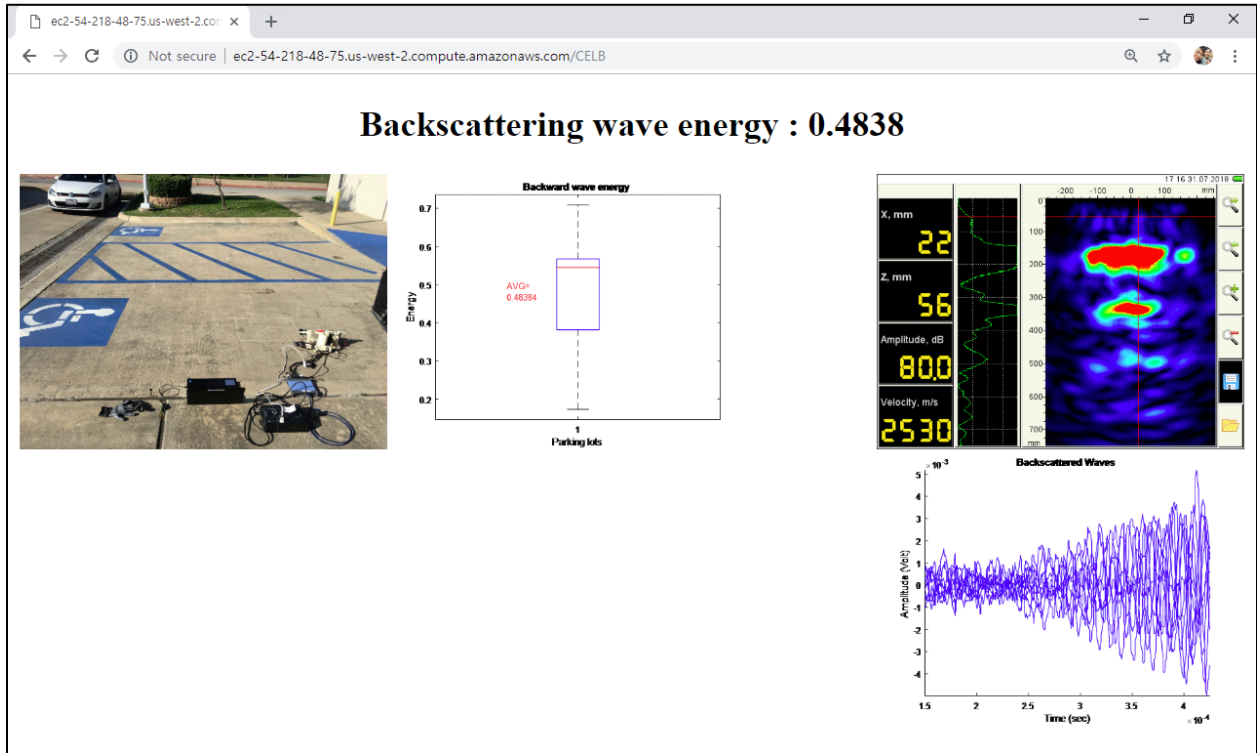
The web pages of the test results are shown in Figure 67. The pages are consisted of the backscattering wave energy value, the picture of field, boxplot of the backscattered wave energy, MIRA test result, and wave forms of the backscattered wave energy.



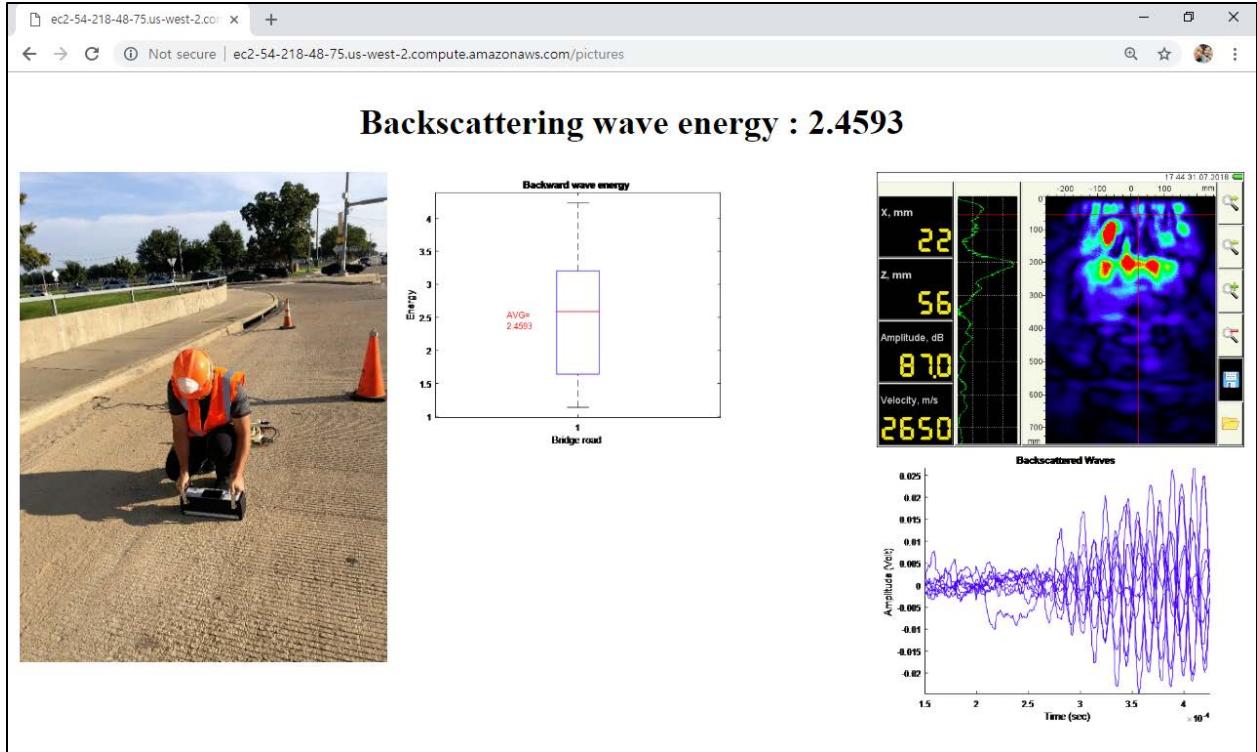
(a) web page of the pedestrian field test result



(b) web page of the recent constructed pedestrian field test result



(c) web page of the parking lots field test result



(d) web page of the bridge road field test result

Figure 67. Web pages of the field test results

7. Conclusions and Recommendations

In this research, the damage and defect detection system of concrete pavement is introduced by conducting laboratory and field tests. In addition, website-based and App-based monitoring platforms are introduced to allow a fast access to the test results using map-based location displayer. Also, the technique of wave backscattering shows high sensitivity in heterogeneous material such as concrete, it is proved that the backscattered energy method is the promised method to detect early age internal damage of heterogeneous materials. However, the more parameter studies about field environments and different concrete mixtures are required to reduce the sensitivity of the backscattered energy method. The web- and App-based monitoring platforms are the promised method to manage any target of infrastructure in an age of high technology by performing real-time monitoring and managing the data.

8. References

- [1] D. Frost, “Long-Term Pavement Performance (LTPP) Data Analysis Support : National Pooled Fund Study TPF-5 (013),” *Fed. Hiw. Adm.*, vol. 5, no. November, 2006.
- [2] A. K. J. F. DEAN J. DESCHENES, OGUZHAN BAYRAK, “ASR/DEF-DAMAGED BENT CAPS: SHEAR TESTS AND FIELD IMPLICATIONS,” 2009.
- [3] S. Ham, H. Song, M. L. Oelze, and J. S. Popovics, “A contactless ultrasonic surface wave Approach to characterize distributed cracking damage in concrete,” *Ultrasonics*, vol. 75, pp. 46–57, 2017.
- [4] E. R. G. K. J. F. J. Z. O. B. K. K. Z. Webb and B. Hanson, “Non-Destructive Evaluation of In-Service Concrete Structures Affected by Alkali-Silica Reaction (ASR) or Delayed Ettringite Formation (DEF)—Final Report, Part I,” 2012.
- [5] K. F. Graff, *Wave Motion in Elastic Solids*. New York: Dover Publications, 1975.
- [6] V. Giurgiutiu, *Structural Health Monitoring with piezoelectric wafer active sensors*, First. South Carolina, Colombia , USA: Elsevier, 2007.
- [7] J. L. Rose, *Ultrasonic guided waves in solid media*. 2014.
- [8] D. Clayton, L. Khazanovich, and L. Salles, *Linear Array Ultrasonic Test Results from Alkali-Silica Reaction (ASR) Specimens*, no. April. 2016.
- [9] J. L. Busse, “Three-Dimensional Imaging Using a Frequency- Domain Synthetic Aperture Focusing Technique,” *IEEE Trans. Ultrason. Ferroelectr. Freq. Control*, vol. 39, no. 2, pp. 174–179, 1992.
- [10] Buck, John R., Michael M. Daniel and ACS. *Computer Explorations in Signals and Systems Using MATLAB*. 2nd Editio. Prentice-Hall, Inc. Upper Saddle River, NJ, USA; 2002.
- [11] Huttenlocher DP, Klanderman GA, Rucklidge WJ. Comparing Images Using the Hausdorff Distance. *IEEE Trans Pattern Anal Mach Intell*. 1993;15(9):850–63.
- [12] Soille P. *Morphological Image Analysis: Principles and Applications*. Springer-Verlag. 1999. 2-3 p.
- [13] Gautam BP, Panesar DK, Sheikh SA, Vecchio FJ. Effect of coarse aggregate grading on the ASR expansion and damage of concrete. *Cem Concr Res*. 2017;95:75–83.
- [14] Ham S, Song H, Oelze ML, Popovics JS. A contactless ultrasonic surface wave approach to characterize distributed cracking damage in concrete. *Ultrasonics*. 2017;75:46–57.

[15] Ham S, Popovics JS. Application of contactless ultrasound toward automated inspection of concrete structures. *Autom Constr.* 2015;58.

Appendix A – Fitted Curve Coefficients

Round aggregates fitted curve coefficients

Agg. Cof.	#1	#2	#3	#4	#5	#6	#7
b1	1.07259	1.55311	1.26360	1.46677	1.13854	1.87814	1.43693
b2	0.26069	0.34876	0.37371	0.61397	0.48385	0.07302	0.48118
b3	0.87333	0.68981	0.45140	-0.62489	-0.00870	0.18901	0.05186
b4	0.21273	0.73311	0.44410	1.41769	0.53675	0.30866	0.66165
b5	0.94997	0.54654	0.82663	1.24375	1.06992	0.53522	1.03916
b6	2.07150	3.33334	2.26264	0.30067	1.18882	1.38332	1.41018
b7	0.06833	0.08686	0.06049	1.17154	0.25286	0.18573	0.19900
b8	1.49811	3.22411	1.19958	1.79561	1.79369	2.21706	1.75923
b9	3.44971	0.38582	4.74591	1.55438	1.64198	1.85559	2.28329
b10	0.01649	0.08741	0.04818	0.97957	0.10406	0.04040	0.06115
b11	2.64112	2.21725	2.90004	2.57589	2.31633	4.10207	2.81989
b12	1.84875	-1.33014	2.29886	2.08181	3.62300	1.80829	2.11658
b13	0.05325	0.04920	0.02005	0.66704	0.07410	0.03592	0.03465
b14	3.84384	4.03496	4.16658	2.82351	3.79708	2.91059	3.75425
b15	3.55998	0.23560	1.08820	4.35177	-0.58863	3.03608	2.30852
b16	0.09101	0.44136	0.01785	0.02669	0.02681	0.00703	0.02878
b17	5.76690	5.05537	5.96801	4.91643	6.02092	4.79129	2.05102
b18	-2.74708	-0.64457	0.97710	2.97246	2.06349	1.10260	3.44516
b19	0.21539	0.01770	0.01474	0.01207	0.01957	0.00715	0.89637
b20	6.22301	7.98636	7.93572	7.62766	7.98983	6.40127	4.73959
b21	-0.91069	2.25905	1.34026	0.14903	1.23520	4.13692	2.21079
b22	0.15544	0.43729	0.01068	0.01365	0.02194	0.00690	0.87996
b23	6.39541	5.10541	10.85193	6.60485	5.48536	12.92775	4.75278
b24	1.71986	2.27890	2.13385	-2.21870	-0.75105	0.42508	5.31249

Crushed aggregates fitted curve coefficients

Agg. Cof.	#1	#2	#3	#4	#5	#6
b1	0.86705	0.97154	1.43238	1.26396	0.96697	1.03536
b2	0.29231	0.39812	0.40847	0.57512	0.34636	0.40064
b3	0.95803	0.07822	0.62636	-0.03159	0.28341	0.59871
b4	0.19512	0.44546	0.66654	2.18327	0.29043	0.38591
b5	0.68929	1.13187	0.71448	1.16883	0.66399	0.84225
b6	3.37367	0.57200	3.13440	1.50710	2.07046	2.63581
b7	0.18883	0.39095	0.12070	1.71230	0.20978	0.03574

b8	2.19676	1.78424	3.00950	1.34067	2.29703	5.30047
b9	0.48998	1.78518	1.73785	4.17409	1.05211	-0.83026
b10	0.09592	0.33902	0.13425	0.11236	0.08322	0.07484
b11	2.84595	2.97391	1.60618	3.24840	4.01350	2.31529
b12	2.53025	0.18047	4.51130	0.86022	2.27376	-1.36223
b13	0.08582	0.04989	0.04728	0.05801	0.08911	0.13122
b14	4.21579	5.54042	3.83039	5.04916	2.99728	3.45941
b15	0.11525	0.79268	2.63206	1.95592	-3.42272	-1.35108
b16	0.06888	0.34023	0.48011	0.02272	0.02996	0.06683
b17	4.93550	3.10919	5.65418	3.97426	4.90267	6.25344
b18	0.94651	2.86889	-0.72346	-2.71750	-2.48954	3.35565
b19	0.03334	0.02304	0.46684	0.02305	0.01434	0.09820
b20	6.90913	6.70515	5.71367	8.02641	6.03078	5.97546
b21	0.17979	-3.92183	2.18681	1.51430	1.95588	0.88506
b22	0.02835	0.01459	0.01161	0.01985	0.01105	0.03173
b23	6.32738	8.35338	12.07811	6.18670	10.01567	7.69334
b24	-1.16434	-2.78066	1.75000	0.45763	0.79125	-0.05852

Needle aggregates fitted curve coefficients

Agg. Cof.	#1	#2	#3	#4	#5	#6	#7	#8
b1	1.68200	1.61471	2.35170	0.90243	9.37699	1.08006	0.91402	3.20847
b2	0.50423	0.69388	0.59959	0.50750	0.37688	0.55980	0.43347	0.03548
b3	-0.16724	-0.46191	-0.41266	-0.02610	1.39283	-0.13386	0.32855	0.07589
b4	0.95513	1.60540	0.96717	0.40991	8.80570	2.52162	0.35005	0.25545
b5	0.69694	1.23781	2.21417	1.00825	0.39905	2.03447	0.80692	0.81514
b6	2.31856	1.08294	0.93359	1.43674	4.50327	1.72583	2.43841	0.63048
b7	0.28028	0.99451	1.80610	0.24775	0.30649	0.60415	0.25608	0.39421
b8	2.37912	2.22973	0.70909	2.00617	1.88176	0.95386	1.92001	1.87748
b9	0.98806	4.46699	2.35407	2.70798	-2.45318	1.81429	-2.41615	0.34870
b10	0.24955	1.37587	0.08599	0.11773	0.06857	0.09566	0.08873	0.07511
b11	2.86176	1.90067	4.20505	3.89179	3.83865	4.09077	4.00090	4.29721
b12	2.11477	2.26453	1.63495	-1.36395	-0.57581	0.72042	-0.39131	-3.17785
b13	0.04161	0.61762	0.68195	0.07308	0.01770	0.04707	0.16846	0.04981
b14	4.36424	4.45377	2.31555	5.01972	3.00468	6.11562	5.88596	3.62018
b15	-1.27550	-2.16930	3.71290	0.65488	0.50810	0.25263	1.96620	0.35650
b16	14.90070	0.55627	0.03229	0.03902	0.02713	2.22135	0.01709	-0.02722
b17	8.51928	4.49930	8.03511	7.01431	6.94199	2.05515	3.05470	6.95645
b18	4.29965	0.88171	-2.25657	2.07198	0.77759	4.85785	0.63811	-4.48754
b19	14.89859	0.02491	0.03285	0.06188	0.02078	0.02251	0.01528	0.03318
b20	8.51836	8.82466	5.97787	3.38305	8.81841	8.10879	10.06006	7.85615
b21	-5.12128	-0.22104	-2.75989	-2.83954	2.64093	-0.36465	1.22176	-1.68666

b22	0.01446	0.02444	0.04346	0.03384	0.01600	0.01410	0.13900	0.02296
b23	6.09595	7.40595	4.82429	6.00136	10.33494	10.01782	5.80171	10.11729
b24	0.53327	-2.49850	3.45707	0.44568	0.15226	-1.17442	-0.92595	2.09839

Appendix B – Procedures for Android App

Step 1

Unzip the project.

1. Unzip the project name “my_first_app.zip”.
2. Copy the folder into AndroidStudioProjects folder.

Step 2

Download and Install Android Studio

<https://developer.android.com/studio/install>

Step 3

Install Gerymotion emulator to run our application (Windows)

1. Go to the *Genymotion download* page.
2. From this page:
 - o download the ready-to-run Genymotion installer for Windows (recommended). This package includes Oracle VM VirtualBox installer.
 - o download the Windows 32/64-bit package. In this case, It must be first download and install **VirtualBox for Windows hosts** from the [Download VirtualBox](#) page.
3. When installing VirtualBox, in the **Custom setup** window, make sure **VirtualBox Networking** is enabled.
4. Save and run the .exe file.
5. Select the setup language and click **OK**. By default, the Genymotion language corresponds to the system language.
6. The Genymotion setup wizard opens. Click **Next**.
7. Select the destination folder by clicking **Browse**. The default destination folder is C:\Program Files\Genymobile\Genymotion. Then click **Next**.
8. Select the start menu folder by clicking **Browse** or check **Don't create a Start menu folder** and click **Next**.
9. Select whether or not to create a desktop icon and click **Next**.
10. Click **Install** and **Finish**.

For more information <https://www.youtube.com/watch?v=MWZ2rVFOQWw>

Step 4

Open project in android studio

1. After installing android studio, open it and click on file at top left.
2. Browsw for the project “my_first_app” and open it.
3. Click on the run button when project gets open.
4. It will ask to select the emulator.
5. Now run the app, it will show this Gerymotion emulator, and select and click on OK.

